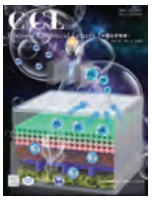
Chinese Chemical Letters 37 (2026) 110791

Contents lists available at ScienceDirect

Chinese Chemical Letters

journal homepage: www.elsevier.com/locate/cclet



# Harnessing chirality: A new dawn in inorganic nanomaterial synthesis and biomedical applications

Yue Pan[a], Jing Ren[a], Yifan Sun[b], Luying Lu[b], Jia Gao[b], Liping Chen[a], Shancheng Yan[a,*], Zhiyang Li[b,*]

[a] School of Chemistry and Life Sciences, School of Integrated Circuit Science and Engineering, Nanjing University of Posts and Telecommunications, Nanjing 210023, China
[b] Department of Laboratory Medicine, Nanjing Drum Tower Hospital, The Affiliated Hospital of Nanjing University Medical School, Nanjing 210008, China

ARTICLE INFO

*Article history:*
Received 28 October 2024
Revised 16 December 2024
Accepted 20 December 2024
Available online 23 December 2024

*Keywords:*
Chiral inorganic nanomaterials
Enantioselectivity
Chiral optical properties
Biomarker detection
Disease therapy

ABSTRACT

Chirality, a fundamental property of biological systems, is widely present at the molecular, cellular, and tissue levels. Current studies have shown that chiral inorganic nanomaterials, have good chiral optical activity as well as high enantioselectivity. When interacting with biological systems, the enantioselective behavior of chiral inorganic nanomaterials towards biomolecules can distinguish between different isomers of biomarkers, which, combined with the excellent optical activity of chiral inorganic nanomaterials, allows for the rapid and sensitive detection of biomarkers. Moreover, chiral inorganic nanomaterials exhibit stronger internalization and retention capabilities in cells, and by specifically targeting specific biomarkers can regulate cellular activity and catalyze related reactions, thereby achieving synergistic treatment of various diseases. In addition, chiral inorganic nanomaterials also have good biocompatibility and do not cause cell damage in living organisms. Moreover, chiral inorganic nanomaterials have programmable surfaces that can be tailored to suit specific biological functions. Due to the important role of chiral inorganic nanomaterials in the biomedical field, this paper summarizes and discusses the synthesis and biomedical applications of chiral inorganic nanomaterials. It further looks forward to its future development prospects to provide a reference for promoting relevant research on chiral inorganic nanomaterials in biomedical fields.

© 2026 Published by Elsevier B.V. on behalf of Chinese Chemical Society and Institute of Materia Medica, Chinese Academy of Medical Sciences.

## 1. Introduction

Chirality refers to the property of an object that cannot be superimposed onto its mirror image through rotation or translation [1]. Chirality is widely present in nature, from the microscopic realm of sugars, amino acids, DNA, and proteins to everyday objects like right-handed snail shells, vines, and spinning windmills to the vast universe. These all exhibit chiral structures, showcasing chirality from the microscopic to the macroscopic scale [2]. Chirality is also common in everyday life, such as the human hands, the tendrils of morning glory, and tree leaves, among others [3]. In addition, a portion of the drugs commonly taken by humans also possess chirality, and living organisms have a precise ability to recognize the chirality of such drugs. The differences in the configuration of chiral drug molecules can result in varying physiological activity and toxicity within the body [4]. Therefore, the investigation of chirality is of significant importance to the well-being of living organisms [5,6].

Chiral nanomaterials will show unique and abundant chiral effects when the chirality is extended from molecular to nanometer or even micrometer size [7,8]. In recent decades, most work has focused on studying chiral organic materials. However, organic chiral nanomaterials are less stable under some specific conditions, which affects their properties and applications [9,10]. Besides, synthesizing organic chiral nanomaterials requires complex processes and high costs, limiting their popularity in large-scale production and applications [11]. Compared with chiral organic nanomaterials, chiral inorganic materials have a chiral lattice and an obvious chiral morphology that can be used as an ideal natural analog [12]. Moreover, chiral inorganic nanomaterials are easy to synthesize, have good biocompatibility, stable optical activity, and physicochemical properties, and are expected to achieve large-scale applications in biomedical fields [13].

Chiral inorganic nanomaterials have seen many applications in various fields of biomedicine. For example, the chiral optical

* Corresponding authors.
*E-mail addresses:* yansc@njupt.edu.cn (S. Yan), lizhiyangcn@qq.com (Z. Li).

https://doi.org/10.1016/j.cclet.2024.110791
1001-8417/© 2026 Published by Elsevier B.V. on behalf of Chinese Chemical Society and Institute of Materia Medica, Chinese Academy of Medical Sciences.

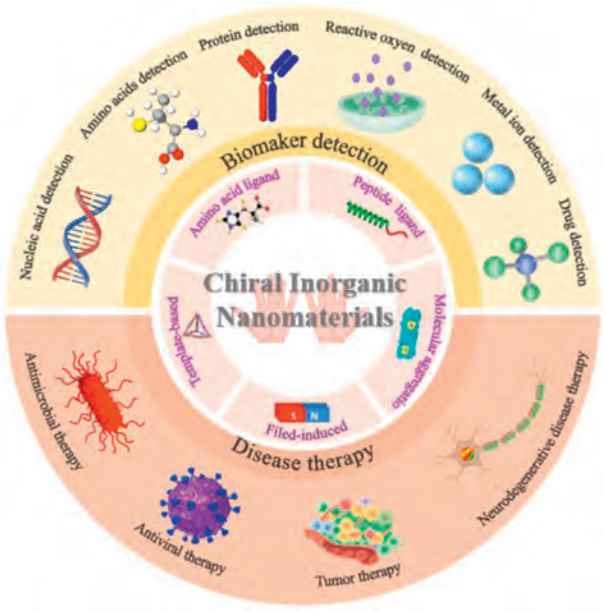



**Fig. 1.** Scheme for the synthesis of chiral inorganic nanomaterials and biomedical application. By Figure Draw. Reproduced with permission [19–22]. Copyright 2016, 2020 and 2024, American Chemical Society.

activity of inorganic nano is utilized for quantitative biomarker detection, chiral differentiation of chiral drugs, and treating a wide range of diseases [14,15]. Specifically, chiral sensing technology can significantly enhance the specificity and sensitivity of biomarker detection [16]. Moreover, chiral nanomaterials can trigger different immune responses in the *in vivo* immune system, providing new ideas for treating immune diseases [17]. In addition, the response of chiral inorganic nanomaterials to light can enhance the therapeutic effects on major diseases [18].

This paper primarily discusses techniques for creating chiral nanomaterials and their uses in the field of biomedicine (Fig. 1) [19–22]. It begins by outlining the key strategies for producing chiral inorganic nanomaterials, then moves on to examine their roles in detecting biomarkers and treating diseases. Lastly, the paper will address the challenges and future possibilities for chiral inorganic nanomaterials in biomedicine. The goal of this thesis is to serve as a useful reference for related research and to promote the exploration and application of chiral inorganic nanoparticles in the biomedical sector.

## 2. Chiral synthesis strategies for inorganic nanomaterials

Ligand-induced and self-assembly methods are mainly used to prepare chiral inorganic nanostructures. The ligand-induced method is mainly used for synthesizing chiral nanoparticles, while the self-assembly method is used for synthesizing chiral nanoassemblies [23]. This section briefly introduces ligand-induced and self-assembly methods based on different chiral synthesis strategies.

### 2.1. Ligand-induced chirality

Ligand-induced directed synthesis of chiral inorganic nanoparticles is a widely used and simple synthesis method [24]. Ligands commonly used for chiral induction of inorganic nanoparticles include amino acids, peptides, and other biomolecules. These biomolecular ligands have good biocompatibility, small size, and ease of functionalization and are therefore widely used in the biomedical field for the synthesis of chiral inorganic nanoparticles [25–28].

#### 2.1.1. Amino acid ligands

Amino acids are one of the smallest components of living organisms, with all amino acids except glycine having a chiral structure [29]. Thus, amino acids are utilized as chiral ligands for synthesizing inorganic nanomaterials. For example, Cao *et al.* [30] used aspartic acid (Asp), valine (Val), glutamic (Glu) acid, and cysteine (Cys) as ligands to enantioselectively synthesize 150 nm chiral perovskite $CsCuCl_3$ nanocrystals (Fig. 2A). The circular dichroism (CD) spectra show a symmetrical CD signal in the range of 400–680 nm, with a peak ± 8 mdeg at 480 nm. Chiral activity can be adjusted by simply adjusting the Cs/Cu feed ratio and amino acid type in the case of the addition of different chiral ligands. Besides, Liu *et al.* [31] synthesized chiral nanoparticles (L/D-$Co_3O_4$) with average sizes of 1.9 nm and 2.2 nm, respectively, in the presence of L/D-histidine (L/D-His), which had mirrored CD signals in the range of 500–800 nm and peaked at 175 mdeg at 535 nm (Fig. 2B). These nanoparticles exhibit significant and tunable chiral optical properties. Analysis by X-ray photoelectron, Fourier transform infrared, and ultraviolet-visible absorption spectroscopy showed that the root cause of its chiral properties was the ratio of $Co^{2+}/Co^{3+}$ and its interaction with the histidine imidazole group. Additionally, Lee *et al.* [32] synthesized chiral cubic gold nanoparticles (L/D-AuNPs) of about 200 nm using chiral cysteine ligands in solution. The L/D-AuNPs have mirrored CD signals in the 300–900 nm range (Fig. 2C). The researchers believe that chiral cysteines can induce optically active Au nanoparticles because they can cause enantioselective interactions at the interface between the nanoparticles and chiral amino acids so that the high-index crystal planes with different chirality have different growth rates and finally develop chiral morphology. Similarly, Li *et al.* [33] reported that chiral cysteine regulates the asymmetric growth of Au NPs in the multilayer $Au/MoS_2$ heterojunction plane and finally forms chiral dendritic Au nanomaterials. The chiral dendritic Au nanocrystals inherit the chirality of cysteine molecules and have a specific recognition function for enantiomer molecules.

In conclusion, amino acids as ligands are readily available and have good biological compatibility. However, amino acids are not easy to modulate the chiral sites of action and chiral properties of chiral inorganic nanomaterials, which tends to result in inhomogeneous nanoparticle sizes. Therefore, modifiable biomolecules are needed as ligands to modulate the chiral nature and nanoscale uniformity of chiral inorganic nanomaterials.

#### 2.1.2. Peptide ligands

The interaction of peptides with nanoparticles can control the growth of nanomaterials and chiral optical properties and is, therefore, also a ligand for inducing chiral synthesis [34]. The ability to modulate the binding capacity of peptide surfaces by changing the peptide sequence allows flexible control of nanomaterials' shape, size, and function [35]. In addition, peptides, as biomolecules commonly used in synthesizing nanomaterials, can enhance nanomaterials' water solubility and biocompatibility [36]. Many chiral nanomaterials have been synthesized using peptides as ligands for induced synthesis. For example, Chen *et al.* [37] utilized chiral cysteine-phenylalanine dipeptides (L/D-Cys-Phe) modification on the surface of gold nanobipyramids with high-index crystal facets to synthesize chiral gold nanobipyramids with sea cucumber-like structures (GBPs) under the action of a reducing agent (Fig. 3A). The $g_{abs}$ (optical anisotropy factor, A parameter for characterizing the chirality of molecules in the ground state) of the synthesized GBPs was measured to be 0.102 at a wavelength of 573 nm. In addition, Chen *et al.* [38] utilized chiral ligand glutathione (L/D-GSH)

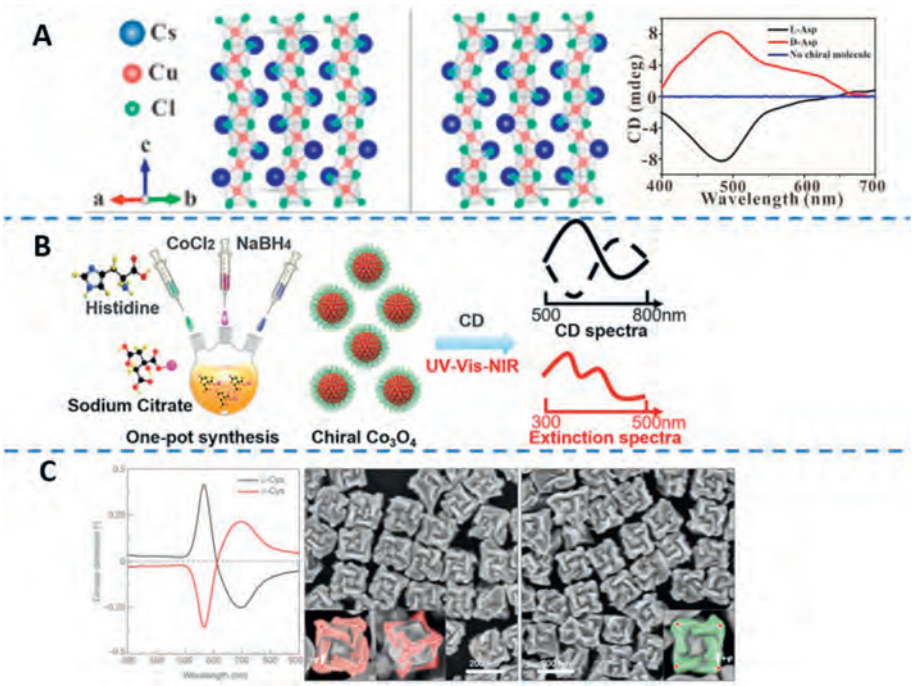



**Fig. 2.** Amino acid-induced synthesis of chiral inorganic nanomaterials. (A) Schematic showing the synthesis and CD signals of chiral $CsCuCl_3$ perovskite-like NCs. Reproduced with permission [30]. Copyright 2023, American Chemical Society. (B) Schematic representation of the one-pot synthesis of chiral $Co_3O_4$@His NPs. Reproduced with permission [31] . Copyright 2023, Wiley-VCH GmbH, Weinheim. (C) CD spectra and SEM image of L/D-Au NPs synthesized using L/D-Cys. Reproduced with permission [33]. Copyright 2022, The Author(s).

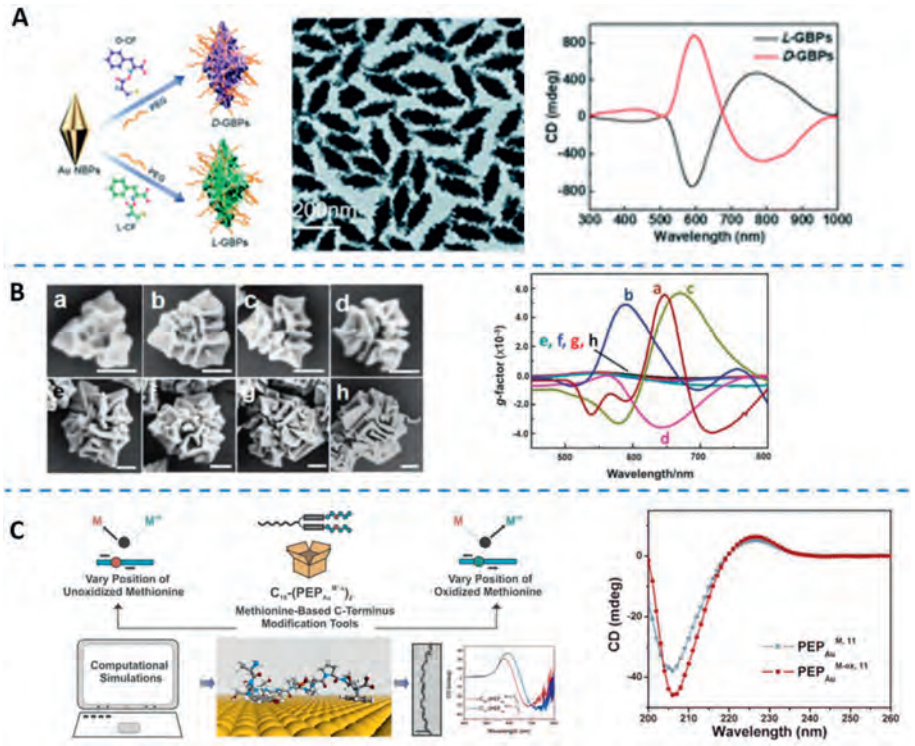



**Fig. 3.** Peptide-induced synthesis of chiral inorganic nanomaterials. (A) Schematic of L/D-GBPs preparation, TEM images, and CD spectra. Reproduced with permission [37]. Copyright 2022, Royal Society of Chemistry. (B) *g*-factor of the nano-badges chiral AuNPs (a-h). Reproduced with permission [38]. Copyright 2023, Wiley-VCH GmbH. (C) Peptide sequence variation for tuning the structure and chiroptical properties of helical Au NPs superstructures. Reproduced with permission [39]. Copyright 2022, American Chemical Society.

**Table 1**
Ligand-induced synthesis of chiral inorganic nanomaterials.

| Ligand | Nanomaterials | Size (nm) | Chirality | Ref. |
|---|---|---|---|---|
| L/D-Trp | Si@D-/L-Trp | ~20 | $g_{abs} = 1.4 \times 10^{-4}$ (348 nm) | [41] |
| L/D-Ser[a] | L/D-C-Dots | 2.0–7.0 | CD = 43 mdeg (212 nm) | [42] |
| L/D-Glu | L/D-Glu-Au | ~50 | CD = 0.8 mdeg (206 nm) | [43] |
| L/D-His | L/D-CdSe@ZnS | 2.5–3.0 | $g_{abs} = 5.8 \times 10^{-3}$ (578 nm) | [44] |
| L/D-Cys | L/D-Cys-$Mo_4O_8$ | 2.9 | $g_{abs} = 7 \times 10^{-3}$ (580 nm) | [45] |
| L/D-(Pen-Phe-Trp) | L/D-$Cu_2S$ | 4 ± 0.5 | CD = 46 mdeg (530 nm) | [46] |
| L-Pyr[b] | CdSe/ZnS | 5.0–9.0 | CD = 4 mdeg (220 nm) | [47] |
| P/M-PANI[c] | P/M-PANI-$Fe_3O_4$ | ~200 | CD = 120 mdeg (450 nm) | [48] |
| L/D-Pen | L/D-CuS | ~20 | $g_{abs} = 2.33 \times 10^{-3}$ (280 nm) | [49] |
| L/D-Tar[d] | L/D-Co superstructures | ~200 | $g_{abs} = 0.033$ (1180 nm) | [50] |
| NALC[e] | L/D-HgS | ~5 | $g_{abs} = 0.015$ (540 nm) | [51] |

[a] L/D-Ser: L/D-Serine acid;
[b] L-Pyr: L-pyroglutamic acid;
[c] P/M-PANI: Nano-fibular polyaniline;
[d] L/D-Tar: L/D-tartaric acid;
[e] NALC: *N*-acetyl-L-cysteine.

to induce the active surface growth of Au on Au nanosheets, resulting in the formation of nano materials with chiral morphology (Fig. 3B). The characteristic of this growth mode is that the growth material is transferred to a few active sites, forming "deep valleys" and "high walls". The authors studied the effect of ligand kinetics by adjusting the concentration of the L/D-GSH, where a decrease in GSH concentration led to a decrease in "high walls" and an increase in the area of flat regions. On the other hand, higher concentrations of glutathione resulted in a decrease in flat regions and a more complex growth pattern.

Besides, Mokashi-Punekar *et al.* [39] demonstrated that peptide sequences can be programmed to control chiral AuNPs' structure and optical activity (Fig. 3C). Experimental evidence showed that the position of the amino acid methionine (M) and the presence of methionine sulfoxide (M-ox) within different peptide sequences (PEPAu = AYSSGAPPMPPF/PEPAu M-ox = AYSSGAPP MoxPPF) in Au-bound peptide conjugate families $C_{18}$-(PEPAu M, x)$_2$ and $C_{18}$-(PEPAu M-ox, x)$_2$ were used to alter the aspect ratio and size of Au NPs within the helical NP assemblies. $C_{18}$-(PEPAu M, x)$_2$ (x = 7, 9, and 11) produced irregular double helical superstructures containing spherical AuNPs, while $C_{18}$-(PEPAu M-ox, x)$_2$ (x = 9, 11) produced single helical superstructures composed of rectangular or rod-shaped AuNPs. Furthermore, when M/M-ox was positioned at x = 11, more significant Au NPs components were observed. In contrast, smaller AuNPs components were observed when M/M-ox was positioned at x = 7. The variations in nanoscale structures were manifested as observable differences in chiral optical signal intensity. Ultimately, the authors achieved significant changes in the structure and properties of chiral Au NPs superstructures through simple molecular-level adjustments of peptide primary sequences.

In conclusion, the synthesis of chiral inorganic nanomaterials from peptides as a programmable ligand can further modulate chiral properties and nanoscale. However, the sequence design and acquisition of peptides are complex and the raw materials are expensive. Therefore, there is a need to develop more convenient means of chiral modulation [40]. In addition, there are also many cases of synthesis of chiral inorganic nanomaterials using the chirality of amino acid molecules or peptide [41–51], which are summarized in Table 1.

### 2.2. Self-assembly chirality

The chiral nature of chiral inorganic nanoparticles is unstable, the optical activity is not easy to regulate, and the synthesis of chiral nano-assemblies using the self-assembly method provides an excellent idea to solve this problem [52]. Chiral nano-assemblies assemble various achiral or chiral nanoparticles into nano-assemblies with strong chiral optical activity [53,54]. Compared with chiral inorganic nanoparticles, chiral nano-assemblies can obtain more stable chiral structures and robust optical activity [55]. The preparation of chiral nano-assemblies can be based on molecular aggregation self-assembly between chiral nanoparticles, external-field inductive self-assembly, and chiral template-promoted self-assembly, described in this section.

#### 2.2.1. Chiral assembly based on molecular aggregation

Molecular aggregation dynamics assembly synthesis of chiral nano-assemblies is performed by optimizing chiral synthesis conditions to increase the molecular distance between nanoparticles, thereby facilitating particle aggregation and assembly [56]. There have been several studies that have capitalized on precisely this. For example, Zhou *et al.* [19] self-assembled L/D-Cys-CdTe NPs as building blocks in an alkaline solution and finally assembled helical superparticles around Te nanowires and obtained chiral activity in the visible range (Fig. 4A). This self-assembly process was severely affected by the oxygen efficiency and pH control. When the assembly process was carried out at a higher pH (pH 11.0), the final assemblies showed the morphology of dense NP chains irregularly attached to the surface of the Te NWs. If the assembly was performed in an oxygen-sufficient atmosphere, the NPs transformed to a deeper oxidation state, forming more Te NWs, and only a few NPs assembled around the Te NWs. Similarly, Yan *et al.* [57] obtained chiral helical nanomaterials by self-assembling L/D-Cys-CdTe NPs in methanol-water mixtures using L/D-Cys-CdTe NPs as building blocks (Fig. 4B). The authors further adjusted $V_{H_2O}$:$V_{MeOH}$ to control the balance between aggregation and decomposition forces of CdTe NPs. The results showed that when $V_{H_2O}$:$V_{MeOH}$ = 1:9, a fiber-like structure appeared, while when $V_{H_2O}$:$V_{MeOH}$ = 1:4, a polydisperse leptospiral nanostructure was formed. When $V_{H_2O}$:$V_{MeOH}$ = 1:1.5, a well-defined polydisperse right-handed helical nanostructure was formed.

In conclusion, the assembly of chiral inorganic nanocomponents based on molecular aggregation dynamics is a simple and convenient method, which requires only the adjustment of pH, oxygen, and raw material ratios to prepare chiral inorganic nanocomponents. However, only a few inorganic nanomaterials are suitable for this preparation method. Therefore, there is a need to develop a more universal chiral assembly method.

#### 2.2.2. Field-induced chirality

External field-induced chiral self-assembly refers to the self-assembly of nanoparticles into chiral structures guided by applying a magnetic field, circularly polarized light, and mechanical forces.

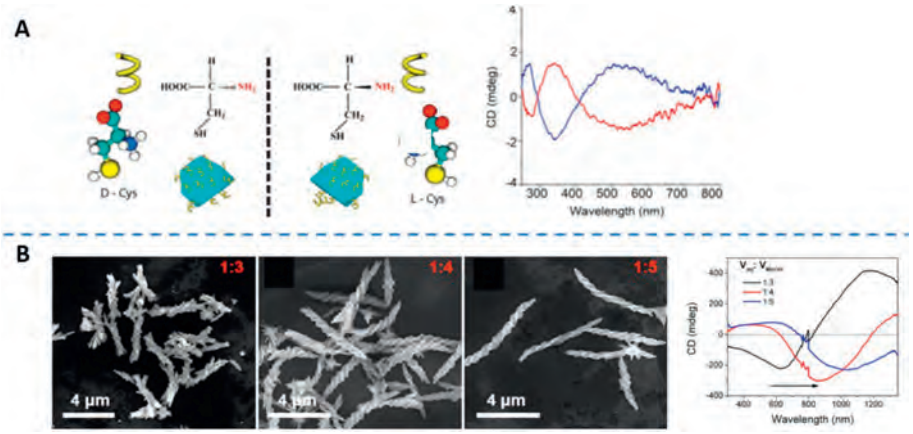



**Fig. 4.** Chiral inorganic nanomaterials assembled *via* intrinsic chiral interactions. (A) Schematic and CD signal characterization of L/D-Cys-CdTe NPs as substrates for self-assembly into chiral superparticles. Reproduced with permission [19]. Copyright 2016, American Chemical Society. (B) $V_{H_2O}/V_{MeOH}$ ratio and their CD signals in the synthesis of different chiral helices. Reproduced with permission [57]. Copyright 2019, American Chemical Society.

A wide range of chiral nano-assemblies can be synthesized easily and conveniently due to the well-tuned magnetic field, circularly polarized light, and mechanical forces [58–60].

Magnetic field-guided chiral assembly of inorganic nanomaterials is based on the principle that inorganic nanomaterials with magnetic properties can be assembled by magnetic dipole-dipole interactions aligned along the magnetic flux using the directionality of the magnetic field [61]. For example, Jeong *et al.* [62] were inspired by astrophysical phenomena to simulate helical magnetic field -assisted self-assembly to construct helical superstructures with chiral properties (Fig. 5A). The authors successfully obtained chiral helical superstructures by using magnetic plasma $Ag@Fe_3O_4$ core-shell NPs as building blocks and directing plasma silver nanoparticles onto the helical magnetic flux, and the chirality of the assembled structures can be switched dynamically and rapidly by adjusting the helical magnetic field. In addition, the authors changed the plasma coupling by controlling the size of silver nanoparticles and the magnetic flux density, thus tuning the CD peak position. Additionally, Wu *et al.* [63] immobilized $Ag@Fe_3O_4$ NPs on polyacrylamide membranes for polymerization and assembly, and used magnetic field-assisted photopolymerization to generate chiral plasma membranes with a thickness of 1 mm using $Ag@Fe_3O_4$ NPs as building blocks (Fig. 5B). The orientation and dispersion of $Ag@Fe_3O_4$ NPs can be controlled by adjusting the magnetic field direction through a cubic permanent magnet to confer chirality to the nanostructures.

Circularly polarized light (CPL)-induced chiral self-assembly refers to the use of chiral nanoparticles that respond differently to left circularly polarized light (LCP) and right circularly polarized light (RCP), which in turn modulates the chirality of the nanocomponents [64,65]. For example, Hao *et al.* [66] co-assembled chiral $FeS_2$ nanoparticles with surface-modified L/D-Cys with chiral hydrogels to form left- and right-handed superhelical structures (L/D-(Gel + $FeS_2$), respectively (Fig. 5C). The assembled chiral gels showed red-shifted CD peaks and significantly enhanced CD signals compared with the original chiral gels, with an asymmetry factor of 0.06, which realized the transfer and amplification of chirality at the molecular level. Moreover, applying LCP or RCP to the chiral gel assemblies could elongate or shorten the pitch of the hydrogels. The pitch values of the helical structures in the hydrogels were between about 149–167 nm under no-light conditions. The pitch values of D-(Gel + $FeS_2$) were increased to 198–213 nm or reduced to 120–131 nm by irradiating D-(Gel + $FeS_{2)}$ with LCP or RCP, respectively, and similar results were obtained using L-(Gel + $FeS_2$) as the test object.

In addition, chiral mechanical forces have also been studied as an extrinsic stimulus for guiding chiral self-assembly, based on the principle that mechanical forces can exert chiral torsional forces on achiral supramolecular nuclei, thereby amplifying the chirality. For instance, Yang *et al.* [67] drop-cast CdSe/CdS nanoparticles with surface-coated aliphatic chains on a substrate and synthesized chiral nano superstructures by mechanical grinding method (Fig. 5D).

In conclusion, the field-induced based approach to synthesize chiral nano-assemblies is simple in the way of regulating the process, universal and less prone to contamination. However, the fine control conditions require high equipment and increase the production cost. Therefore, there is a need to develop a chiral nanocomponent synthesis method that is both universal and cheap and convenient.

### *2.2.3. Template-based chiral assembly*

Template-based chiral assembly refers to the use of a template that provides a chiral conformation, and inorganic nanoparticles "inherit" the chirality of the template by attaching or growing on the chiral template [68,69]. Since the source of chirality is the template and there are not many restrictions on the inorganic nanoparticles, this method is also the most widely used method for preparing chiral nano-assemblies [70,71]. In nanomedicine, commonly used templates are DNA, peptides, *etc.*

DNA, a commonly used chiral template, is thermodynamically stable and mechanically rigid and can be formed into different topologies such as spherical, ring-shaped [72]. For example, Chen *et al.* [73] synthesized chiral dimeric Au nanorods (NR) and chiral trimeric Au NR using DNA origami as a template (Fig. 6A). The chiral optical response of the Au NR trimer was confirmed by CD spectroscopy to be the sum of the chiral optical responses of all Au NR dimers. Besides, Lan *et al.* [74] synthesized chiral plasmonic helical structures of Au nanorods by self-assembling DNA as a template (Fig. 6B). The geometry of DNA origami monomers was dynamically adjusted by rationally designing DNA strand displacement reactions. For example, dynamic modification of the inter-arm angle of a V-shaped DNA origami monomer transforms its chiral superstructure from a tightly folded state with a small inter-rod dihedral angle to a stretched state with a sizeable inter-rod angle. Upon structural remodeling, the amplitude and frequency of the plasmonic chiral signal are reversibly altered. At the same time, the plasma chiral signal was reversed by dynamically changing the DNA origami monomer into its mirror structure and transforming the Au NR chiral superstructure into its mirror structure. The advantage of using DNA as a chiral template is DNA's well-

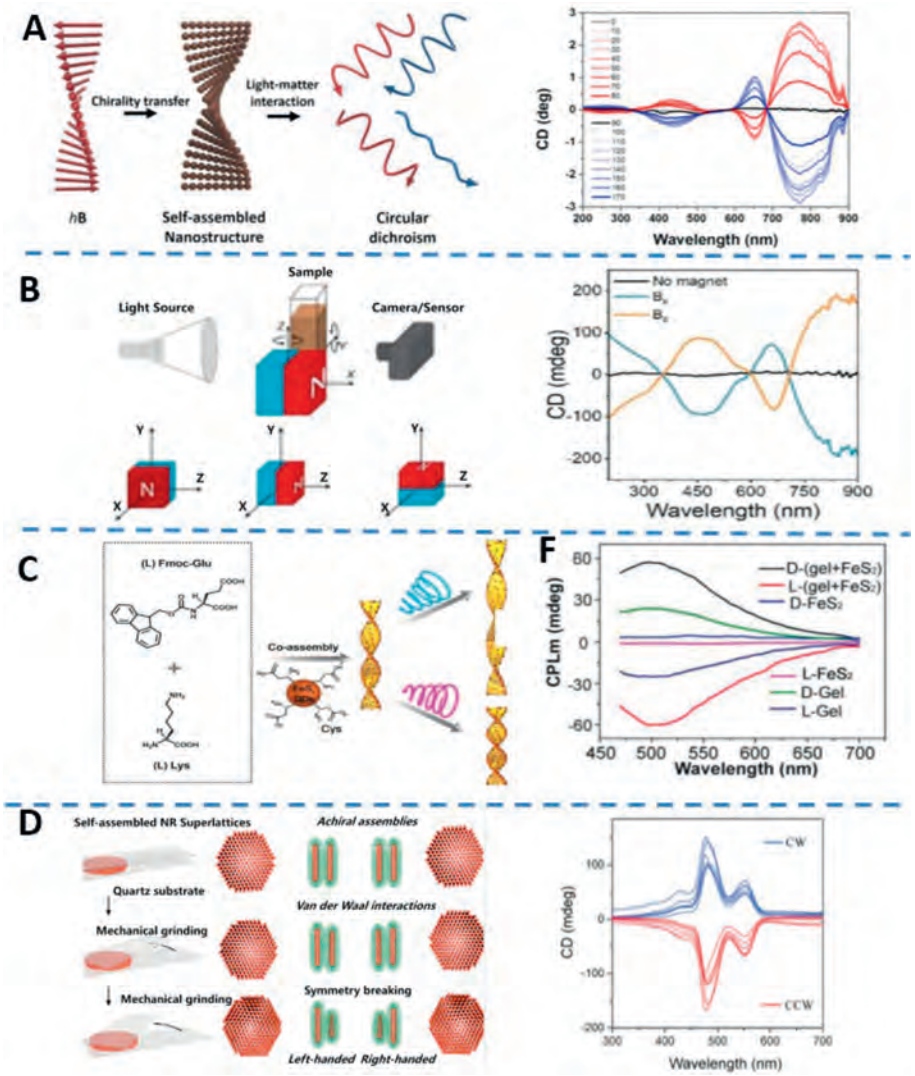



**Fig. 5.** External field-induced assembly of chiral inorganic nanomaterials. (A) Scheme of hB-induced chiroptical property and CD spectra of assembled MagPlas superstructures with varying $\theta$ ($0° \leqq \theta < 180°$). Reproduced with permission [62]. Copyright 2020, American Chemical Society. (B) Schematic illustration of the setup for measuring the extinction and CD spectrum of particle dispersion under a chiral magnetic field and CD spectra of the Ag@$Fe_3O_4$ NPs. Reproduced with permission [63]. Copyright 2023, Royal Society of Chemistry. (C) The illustration of the cogel formation and its CPL responsiveness and CPL emission spectra of cogels excited at 400 nm. Reproduced with permission [66]. Copyright 2019, Wiley-VCH Verlag GmbH & Co. KGaA, Weinheim. (D) Schematic illustration and CD spectra of the chirality generation in self-assembled nanorod super-lattices through a press-and-rotate mechanical force. Reproduced with permission [67]. Copyright 2022, The Author(s).

established and tight molecular recognition, making the assembly process highly selective [75]. In addition, using modern biology and molecular biology techniques, DNA can be tailored into different sequences, lengths, and shapes and chemically modified with different functional groups, possibly preparing nanodevices with specific properties and requirements [76,77].

Protein molecules with different functions are formed by precisely controlling the sequence and folding of the amino acids in a polypeptide [78]. Because peptides have a higher degree of programmability than individual amino acids, peptides can be designed to control the assembly of nanomaterials into complex topologies [79]. Lu *et al.* [80] co-assembled Au NR with human islet amyloid polypeptide (hIAPP), and the supramolecular interaction between the Au NR and the adsorbed hIAPP could transform the hIAPP from high-energy random nematic clusters to low-energy folded structures, which could facilitate and accelerate the fibrillization process (Fig. 6C). Moreover, the Au NR adsorbed with hIAPP on the surface can be further co-assembled with hIAPP in the solution to construct ordered nanospiral fiber structures with lengths of tens or hundreds of micrometers. Additionally, Liu *et al.* [81] reported the coordination assembly of ferrocene-diphenylalanine (Fc-FF) with divalent copper ions ($Cu^{2+}$) into a metal peptide assembly (MPA) with a hierarchical helical structure. The MPA consists of helical nanofibers with hierarchical porous structure and abundant Fc and $Cu^{2+}$ active sites. It exhibits higher catalytic activity for the decolorization reaction than natural laccase. In addition, a series of multistructured MPAs can be synthesized by controlling the temperature and enantiomeric excess (*ee*). Peptide enantiomers with higher *ee* values will self-assemble into highly complex and ordered structures with higher surface areas and porosities than those assembled by peptides with lower *ee* values, leading to enhanced catalytic activity. These results provide new insights into the important role of chirality in guiding the self-assembly of biomolecules into highly ordered and complex functional structures. the advantage of using DNA and peptides as templates for chiral assembly is that it facilitates the formation of highly ordered chiral structures. The template-based method for the synthesis of chiral inorganic nanocomponents is simple and convenient, with a wide range of applicability, and can precisely control the size and shape and structural properties of nanomate-

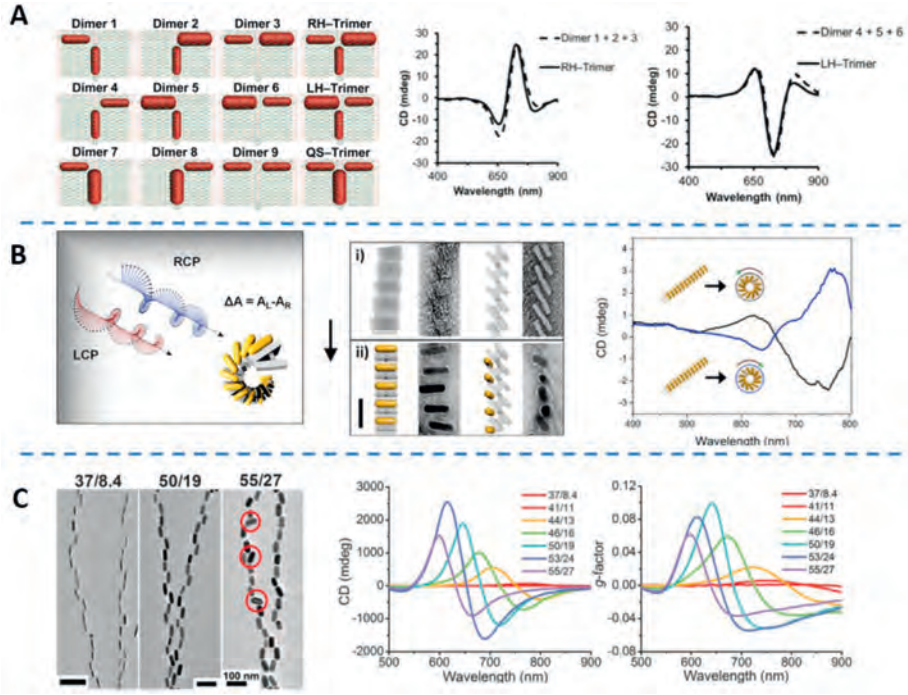



**Fig. 6.** Chiral inorganic nanomaterials are assembled using the template method. (A) Schematic and CD spectra of the synthesis of Au trimers using DNA origami as a template. Reproduced with permission [73]. Copyright 2018, American Chemical Society. (B) Schematic interaction between incident CPL and Au NR chiral superstructure and TEM images and CD spectra of Au NR. Reproduced with permission [74]. Copyright 2018, American Chemical Society. (C) CD spectra, *g*-factor spectra, and representative TEM images for helices from various sizes of NRs assembled under identical conditions. Reproduced with permission [80]. Copyright 2021, American Association for the Advancement of Science.

**Table 2**
Self-assembly synthesis of chiral inorganic nanomaterials.

| Self-assembly method | Nanomaterial | Size | Chirality | Ref. |
|---|---|---|---|---|
| Molecular aggregation self-assembly | L/D-CdS/CdTe | ~1 μm | CD = 10 mdeg (220 nm) | [82] |
| Molecular aggregation self-assembly | SOBU/Au5 tubular nanocomposites | ~37.5 nm | CD = 140 mdeg (650 nm) | [83] |
| CPL | L/D-Au | 10–15 nm | CD = 1.0 mdeg (485 nm) | [84] |
| CPL | L/D-Au/$TiO_2$ nanostructures. | 40–110 nm | CD = 20 mdeg (560 nm) | [85] |
| Magnetic field | L/D-$Fe_3O_4$@$SiO_2$/$CsPbB_3$ | ~100 μm | CD = 125 mdeg (400 nm) | [86] |
| Template | DNA1–Au NR | 10 nm | CD = 3.2 mdeg (665 nm) | [87] |

rials. However, it also faces the disadvantages of template stability as well as high requirements for the synthesis system. Future research needs to address these issues in order to give full play to the advantages of the template method. In addition, there are some examples of self-assembly approaches to synthesis chiral inorganic nanomaterials shown in Table 2 [82–87].

In summary, we present the two core strategies of ligand-induced and self-assembly methods for chiral inorganic nanomaterials, and introduce a series of chiral inorganic nanomaterials synthesized by common amino acids, peptide-induced as well as by molecular aggregation, external-field and template-based methods of self-assembly. After discussing strategies for synthesizing chiral inorganic nanomaterials, we next summarize and discuss examples of biomedical applications of these materials in Section III.

## 3. Biomedical applications of chiral inorganic aanomaterials

Applying chiral inorganic nanomaterials in biomarker detection and disease therapeutics exhibits some unique advantages. In biomarker detection, chiral inorganic nanomaterials can utilize their chiral properties as chiral sensors or probes to specifically recognize and bind chiral biomolecules, improving the accuracy and sensitivity of detection [88]. Through surface functionalization, chiral inorganic nanomaterials can enhance the affinity for specific biomarkers and achieve precise and selective detection [89]. In terms of disease treatment, the physical and chemical properties of chiral inorganic nanomaterials can be utilized for chemodynamic therapy (CDT) and immunotherapy, and the optical activity of chiral inorganic nanomaterials can be utilized for photodynamic therapy (PDT) or photothermal therapy (PTT) to enhance the therapeutic effect of diseases [90,91].

### 3.1. Biomarker detection

The detection of biomarkers is essential in the biomedical sector. The chiral optical properties and high enantioselectivity of chiral inorganic nanomaterials are significant for identifying biomarkers. These nanomaterials can selectively bind to or catalyze biomarkers, and by integrating signals from Raman spectroscopy, fluorescence, and circular dichroism, the specificity and sensitivity of biomarker detection can be greatly enhanced, allowing for extremely sensitive trace detection in biomedical applications. This section examines the use of chiral inorganic nanomaterials for the targeted detection of various biomarkers, including nucleic acids, amino acids, proteins, reactive oxygen species, metal ions, and drug enantiomers.

#### 3.1.1. Nucleic acid detection

Nucleic acid detection is vital in the early and rapid diagnosis of infectious diseases, screening, and diagnosis of genetic dis-

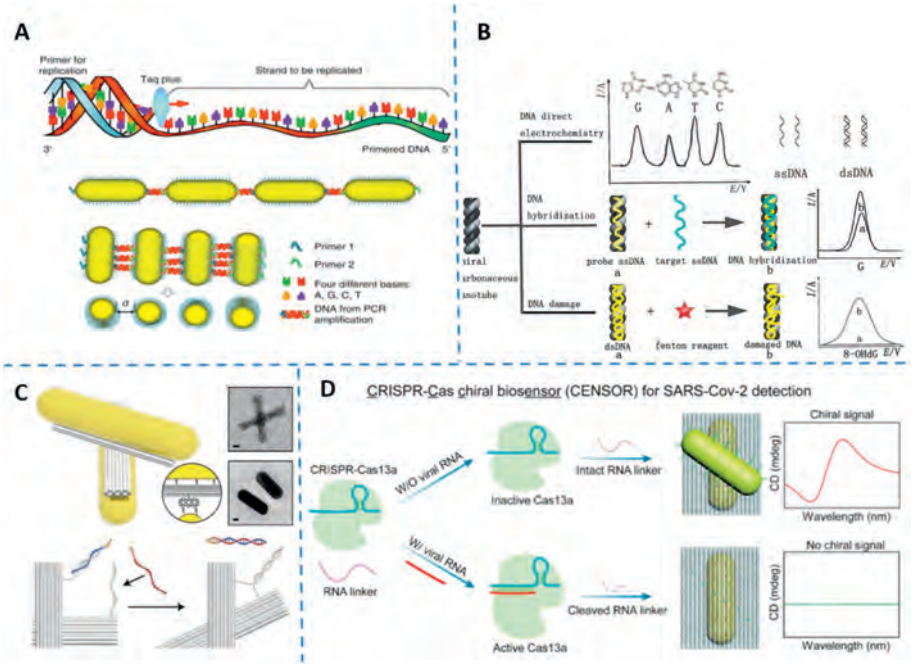



**Fig. 7.** Chiral inorganic nanomaterials for nucleic acid detection. (A) Schematic diagram of PCR-based end-to-end assembly and side-by-side assembly of Au NR. Reproduced with permission [94]. Copyright 2013, The Author(s). (B) Nitrogen-doped Chiral-CNT is used for ultrasensitive DNA direct electrochemistry, DNA hybridization, and damage study. Reproduced with permission [95]. Copyright 2013, Elsevier B.V. (C) Schematic of the mechanism of RNA recognition by DNA origami-assembled Au NR. Reproduced with permission [96]. Copyright 2018, Wiley-VCH Verlag GmbH & Co. KGaA, Weinheim. (D) Schematic of the combined detection of SARSCov-2 RNA by CRISPRCas and chiral biosensors. Reproduced with permission [97]. Copyright 2023, Elsevier B.V.

eases [92,93]. Chiral inorganic nanomaterials are used mainly by two methods for detecting nucleic acid molecules (DNA and RNA sequences). The first one is to assemble chiral inorganic nanomaterials using DNA as a template and to detect DNA sequences by coupling and amplifying the detection signal using surface plasmon excitations of chiral inorganic nanomaterials. In this case, DNA serves as a chiral template and a nucleic acid molecular recognition site. The second is to combine CRISPR-Cas technology to detect RNA sequences by changing chiral signals after pre-amplification of RNA targets. For example. Ma *et al.* [94] realized the construction of chiral dimer structures by DNA-mediated side-by-side assembly using Au NR as the matrix elements (Fig. 7A). The surface plasmon exciton coupling between two Au NR can lead to a powerful localized electromagnetic field hot spot effect. This dramatically enhances the electrochemical photoluminescence (ECL) signal. In addition, DNA strands can regulate the distance between dimers and serve as binding sites for nucleic acid molecular sensing. Experimental results show that the amplitude of the double signals in the circular dichroism spectrum of this nano-assembly exhibits an excellent linear relationship with the amount of target DNA. This technique reduced the DNA detection limit to 3.7 amol/L. Cui *et al.* [95] constructed a novel, simple, and sensitive label-free electrochemical DNA biosensing platform based on novel nitrogen-doped chiral carbon nanotubes (Chiral-CNT) for biosensing studies of DNA bases, DNA hybridization, and DNA damage (Fig. 7B). Due to the unique helical structure of chiral carbon nanotubes, direct electrochemical detection of DNA tetrabases, single-stranded DNA, and double-stranded DNA can be achieved without the need for a prehydrolysis process. This electrochemical DNA biosensing platform enables qualitative and quantitative DNA hybridization detection with a minimum detection limit of 0.0268 g/L. In addition, using 8–hydroxy-2 deoxyguanosineas the electrochemical signal, Chiral-CNT can effectively detect Fenton's reagent-induced DNA damage, with a detection limit of 0.0350 mg/mL and a sensitivity of 7.42 μA mL/mg.

In another study, Funck *et al.* [96] constructed a three-dimensional Au-DNA hybrid chiral nanostructure. The recognition region of the sensor consisted of two oligonucleotides located at one end of each arm of the nanostructure (Fig. 7C). These two sequences were designed as complementary locking strands, forming one of the two locking strands into a blocking strand to prevent premature locking of the structure. Removal of the blocking strand by strand displacement can lock the structure in a right-handed chiral state when a match to a target RNA sequence in the hepatitis C virus genome is present, resulting in a strong circular dichroism signal. This approach reduces the nucleic acid detection limit to 100 pmol/L, demonstrating its excellence in highly sensitive nucleic acid detection. Besides, Yu *et al.* [97] combined a plasma chiral biosensor with CRISPR-Cas13a, capable of sensitively and specifically detecting SARS-CoV-2 RNA (Fig. 7D). The chiral biosensor was designed on a DNA origami template by assembling Au NR into a chirally controllable three-dimensional plasma structure. This modular assembly enhances the flexibility and adaptability of the sensor, thereby increasing its versatility as a sensing platform. In the presence of SARS-CoV2 RNA, the CRISPR-Cas13a enzyme triggers the side-cutting of the RNA molecule, resulting in a different chiral signal read by the biosensor than in the absence of the RNA target present. Notably, even a small change in the concentration of SARS-CoV-2 RNA caused a significant change in the chiral signal after preamplification of the RNA target, with a detection limit of 0.133 amol/L.

### *3.1.2. Amino acids detection*

Amino acid detection is an important topic in biomedicine [98]. In living organisms, except for glycine, other Amino acid can be categorized into L- and D-types, which are involved in different biochemical processes and have different physiological significance [99]. Chiral inorganic nanomaterials for amino acid detection are divided into three main categories; the first is the preparation of molecularly imprinted chiral inorganic nanomaterials for amino

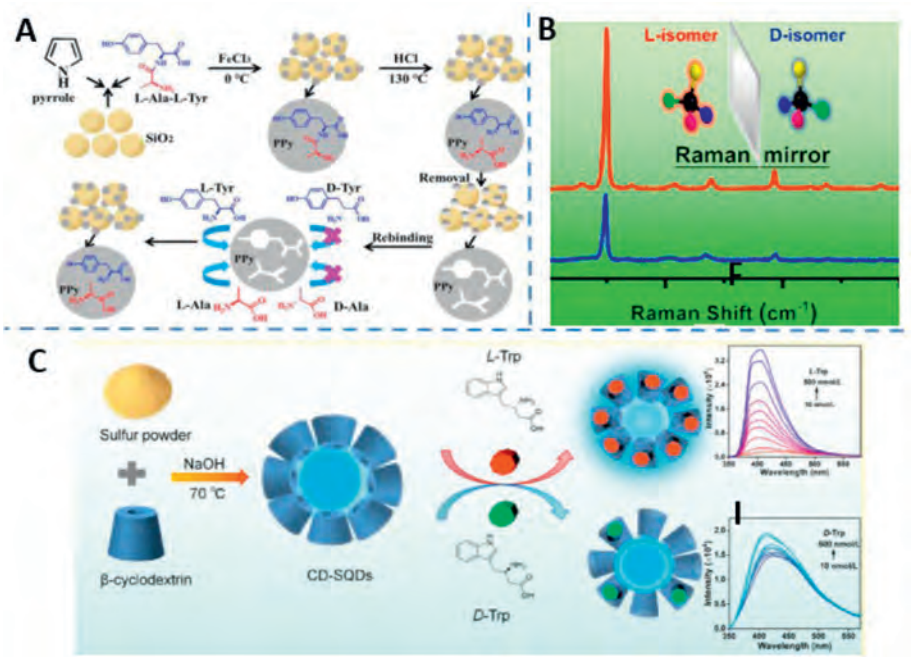



**Fig. 8.** Chiral inorganic nanomaterials for amino acid detection. (A) Basic strategy for preparing L-Ala and L-Tyr co-imprinted $SiO_2$/PPy. Reproduced with permission [100]. Copyright 2019, American Chemical Society. (B) Schematic representation of L/D-$SiO_2$/PDA Raman spectroscopy for detecting L/D-Cys. Reproduced with permission [101]. Copyright 2020, American Chemical Society. (C) Schematic representation of CD-SQD-based chiral sensing strategy. Reproduced with permission [102]. Copyright 2023, American Chemical Society.

acids. The second one utilizes Raman anisotropy between chiral inorganic nanomaterials and amino acid enantiomers as the primary detection principle. The third one utilizes the enantioselective catalytic property of chiral inorganic nanomaterials. Chiral inorganic nanomaterials have also been the subject of many studies in quantitatively determining amino acids. For example, Kong *et al.* [100] prepared a chiral sensor ($SiO_2$/PPy) with L-Ala and L-Tyr imprints. This sensor can simultaneously recognize the chirality of L/D-alanine (L/D-Ala) and L/D-tyrosine (L/D-Tyr) (Fig. 8A). This work opens a new avenue for the simultaneous detection of two or more chiral amino acids, avoiding the drawbacks encountered with multi-template molecular blotting techniques by incorporating only one template.

Besides, Kong *et al.* [101] performed enantioselective recognition of amino acid enantiomers using polydopamine-modified chiral $SiO_2$ nanofibers (L/D-$SiO_2$/PDA). The Raman scattering intensity of the cysteine enantiomer was more than twice that of the enantiomer with opposite chirality. Similar results were found in Cys, Phe, and Tyr enantiomers (Fig. 8B). Additionally, Jiang *et al.* [102] investigated a chiral sensing system of $\beta$-cyclodextrin ($\beta$-CD)-coated sulfur quantum dots (CD-SQDs) for enantioselective fluorescence recognition of tryptophan (Trp) (Fig. 8C). CD-SQDs selectively recognizing L-Trp were prepared by taking advantage of the different binding capacities between L/D-Trp and $\beta$-CD. The addition of L-Trp and the stereoselective catalysis of CD-SQDs enzyme mimics increased the fluorescence intensity of the CD-SQDs, which showed a linear response in the range of 10–500 nmol/L, with a detection limit of (LOD) 2.3 nmol/L. The CD-SQDs were effective for commercial L-Trp in complex amino acid injection and showed good selectivity.

### 3.1.3. Protein detection

Protein markers can be used as indicators of the presence and severity of disease [103]. Therefore, the detection of protein markers is important for the early diagnosis of diseases. The detection of protein markers by chiral inorganic nanomaterials is based on two strategies: one is to immobilize protein antibodies on chiral inorganic nanomaterials to specifically recognize the target proteins, and use the chiral signals of the chiral inorganic nanomaterials as the detection signals to quantify the detection. The other is to utilize the chiral plasmonic nature of some chiral inorganic nanomaterials to have different affinities for different folding states of proteins and thus detect the protein structure. For example, Wang *et al.* [104] developed a biosensor based on a chiral assembly of Au NP trimers for the detection and quantification of the major shellfish allergen tropomyosin (TROP) (Fig. 9A). TROP and an anti-TROP monoclonal antibody were immobilized on 20 nm and 30 nm 16-mercaptohexadecanoic acid (16-MHDA)-functionalized Au NPs to assemble trimers with CD signals. Free TROP in the samples was quantified as an Au NP trimer formation inhibitor. The Au NP trimer-based biosensor selectively determined TROP in the range of 0.1–15 ng/mL with LOD of 21 pg/mL ($S/N = 3$) and a limit of quantification (LOQ) was 70 pg/mL ($S/N = 10$). In addition, Wang *et al.* [105] synthesized chiral triangular gold nanorings (L/D-Pt@AuTNR) through a self-assembly process (Fig. 9B). This nanostructure leverages the selective resonant coupling between induced electric and magnetic dipoles, which are associated with enantiomeric and chiral plasmas, to facilitate the detection of A$\beta$ monomer and protofibrils *via* surface-enhanced Raman scattering (SERS). Consequently, the detection limits for these markers were significantly lowered to 0.045 amol/L and 4 pmol/L, respectively.

### 3.1.4. Reactive oxygen species detection

Reactive oxygen species (ROS) are by-products of biological aerobic metabolism and are a general term for a group of reactive oxygen-containing substances in nature [106,107]. ROS plays a double-edged role in living organisms, with low levels of ROS regulating a wide range of physiological activities. At the same time, excessive accumulation of ROS triggers a series of oxidative damages, leading to the development of a wide range of diseases [108,109]. The main principle of chiral inorganic nanomaterials for reactive oxygen species detection is that reactive oxygen species can oxidize the surface of chiral nanoparticles, thus altering the chiral or fluorescent signals of the nanomaterials, *etc.* For instance,

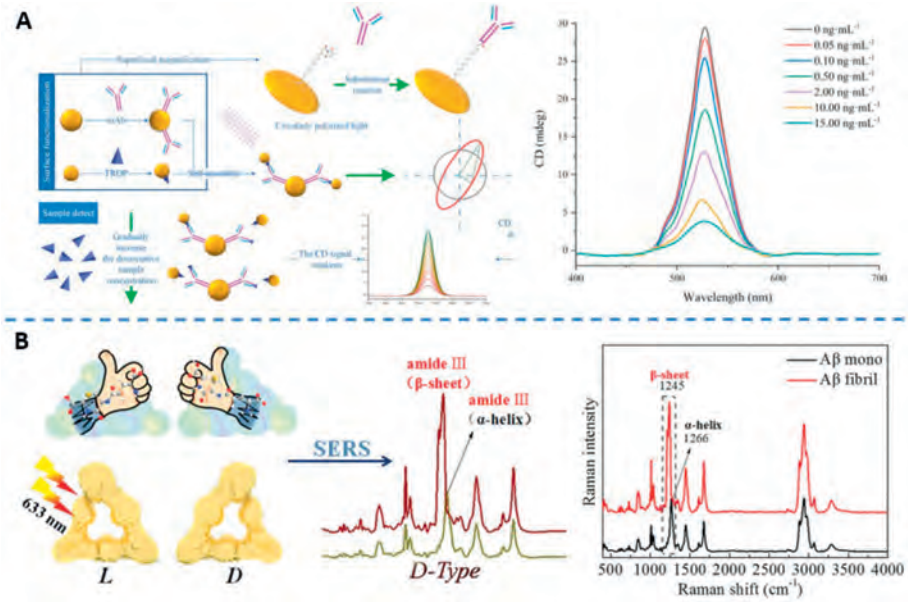



**Fig. 9.** Chiral inorganic nanomaterials for protein detection. (A) Schematic illustration for the Au NP trimer-based biosensor for TROP detection and the CD absorption curves of TROP standards with increasing concentration. Reproduced with permission [104]. Copyright 2019, Elsevier B.V. (B) Schematic illustration for L/D-Pt@Au TNRs used as label-free SERS substrates for A$\beta_{42}$ detection and Label-free SERS spectra of D-Pt@Au TNRs with A$\beta_{42}$ monomers and fibrils. Reproduced with permission [105]. Copyright 2021, Wiley-VCH GmbH.

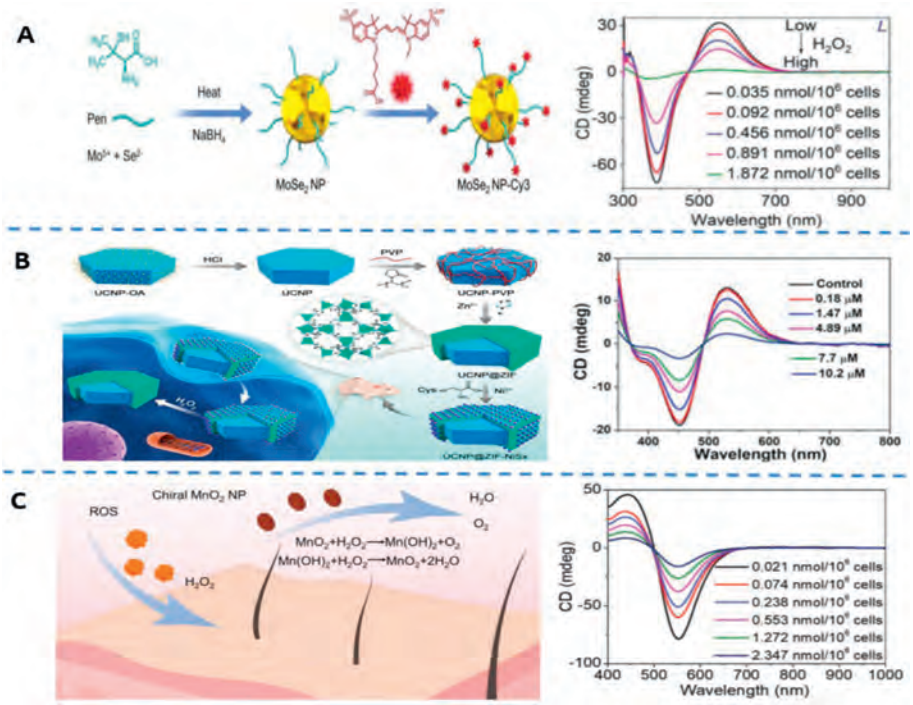



**Fig. 10.** Chiral inorganic nanomaterials for reactive oxygen species detection. (A) Schematic of the synthesis of chiral $MoSe_2$ nanoprobes and CD spectra of HeLa cells pretreated with chiral $MoSe_2$ nanoparticles reacting with different concentrations of $H_2O_2$. Reproduced with permission [110]. Copyright 2023, Wiley-VCH GmbH. (B) Principle of ROS detection using UCNP@MOF-$NiS_x$ nano-assemblies and CD spectra of Hela cells pretreated with the probes at different concentrations of $H_2O_2$. Reproduced with permission [111]. Copyright 2019, American Chemical Society. (C) Schematic of chiral $MnO_2$ NPs used to scavenge ROS *in vivo* and CD spectra of HaCaT cells pretreated with chiral $MnO_2$ NPs at different concentrations of $H_2O_2$. Reproduced with permission [112]. Copyright 2023, Wiley-VCH GmbH.

Cao *et al.* [110] constructed a novel probe based on chiral $MoSe_2$ NPs modified with the fluorescent cyanidin 3 (Cy3) (Fig. 10A). These chiral $MoSe_2$ NPs would exhibit strong CD signals at 390 nm and 550 nm, while the $MoSe_2$ NPs burst the fluorescence signal of Cy3 at 560 nm. In the presence of ROS, the novel probe was rapidly oxidized upon reaction with ROS, resulting in a decrease in the CD signal, while the Cy3 fluorescence signal was restored. With the help of CD and fluorescence bimodal signals associated with ROS, the LOD of CD and fluorescence signals of this nanoparticle in living cells were 0.0093 nmol/$10^6$ cells and 0.024 nmol/$10^6$ cells, respectively. In complex biological environments, this nanoparticle exhibited high selectivity and sensitivity to ROS, which was also consistent with the fact that NPs $Mo^{4+}$ and $Se^{2-}$ oxidation reactions were on the surface. In addition, the chiral $MoSe_2$ NPs were

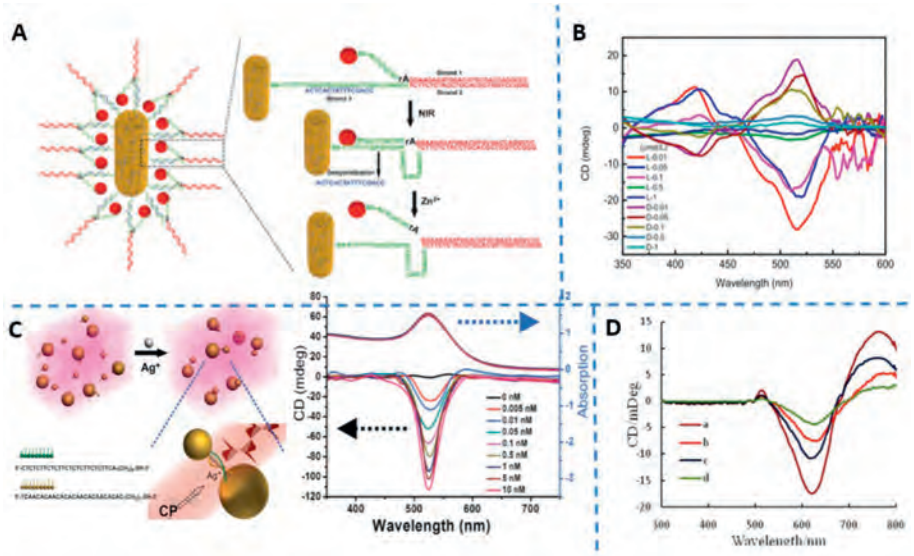



**Fig. 11.** Chiral inorganic nanomaterials for metal ion detection. (A) Working principle of the YSNR@Au NPs core-satellite assembly for $Zn^{2+}$ detection. Reproduced with permission [113]. Copyright 2018, Wiley-VCH Verlag GmbH & Co. KGaA, Weinheim. (B) Chiral CdSe nanoplatelets as an ultrasensitive probe for $Pb^{2+}$ sensing. Reproduced with permission [114]. Copyright 2019, Royal Society of Chemistry. (C) Schematic of $Ag^{+}$ detection based on Cyt-Ag-Cyt recognition and CD spectroscopy. Reproduced with permission [115]. Copyright 2013, Wiley-VCH Verlag GmbH & Co. KGaA, Weinheim. (D) CD spectra of end-to-end and side-by-side assembled Au NR in assembled Au NR with and without $Cu^{2+}$. Reproduced with permission [116]. Copyright 2017, Elsevier B.V.

also able to monitor ROS levels *in vivo via* fluorescent signaling. Additionally, Hao *et al.* [111] prepared nanohybrid assemblies consisting of upconversion nanoparticle (UCNP) cores and zeolite imidazolate backbone structural material-8 (ZIF-8) shells encapsulated with chiral NiSx NPs (UCNP@ZIF-NiSx) (Fig. 10B). Using hydrogen peroxide ($H_2O_2$) as a model validation target in living cells, the results showed that with the degradation of NiXs, the UCNP@ZIF-NiSx nano-assemblies turned into UCNP@ZIF nanocomponents and were successfully quantitatively and selectively detected for ROS *in vivo*. Moreover, Qu *et al.* [112] designed and synthesized chiral $MnO_2$ NPs with dual signals of CD and magnetic resonance imaging (MRI) response to ROS (Fig. 10C). CD and MRI signals exhibited an excellent linear range for intracellular $H_2O_2$ concentration, with LOD of 0.0027 nmol/$10^6$ cells and 0.016 nmol/$10^6$ cells, respectively.

### 3.1.5. Metal ion detection

Metal ions have many important physiological functions in living organisms, so detecting metal ions has important biological significance. The principle of metal ion detection by chiral inorganic nanomaterials is that the addition of metal ions affects the chiral structure of chiral inorganic nanomaterials, which in turn affects the chiral signal [113–116]. In the current study, the primary metal ions detected by chiral inorganic nanomaterials, including Zn ions, Pb ions, Ag ions, Cu ions. For example. Hao *et al.* [113] synthesized Au@AgAu core-shell nanorods (YSNRs) with tunable plasma circular dichroism (PCD) response using chiral penicillamine (L/D-Pen) and Au@AgAu assembled with Au nanoparticles to construct a YSNR@ Au NP core-satellite (CS) assembly with enhanced PCD intensity and *g* factor (Fig. 11A). After near-infrared (NIR)irradiation, the PCD responses of the CS assemblies at 530 nm and 740 nm were almost unchanged without adding $Zn^{2+}$. In contrast, in the presence of $10 \times 10^{-3}$ mol/L $Zn^{2+}$, the CD peak at 530 nm almost disappeared, and the CD response at 740 nm weakened, suggesting disintegration of the CS structure due to $Zn^{2+}$. Concentration gradient experiments showed a good linear relationship between the CD signal and the $Zn^{2+}$ concentration in the range of 0.1–20 μmol/L. The CD signal also responded well to the $Zn^{2+}$ concentration. It was further used for the intracellular detection of $Zn^{2+}$ in Parkinson's disease cells, and the sensitivity could reach $38.7 \pm 0.3 \times 10^{-6}$ mol/L/$10^6$ cells.

In addition, Chen *et al.* [114] induced the synthesis of ultrathin chiral CdSe nanosheets using L/D-Cys as chiral ligands (Fig. 11B). The chiral ligands transferred their chiral optical activity to the achiral nanosheets with an anisotropy factor of $10^{-4}$, which induced chiral exciton jumps. It was found that the CD intensity response of such chiral nanosheets at 520 nm showed a significant linear relationship with the logarithmic concentration of lead ions, with correlation coefficients of 0.998 and 0.994, respectively. The experimental LOD for lead ion sensing was $4.9 \pm 0.3$ nmol/L.

Besides, Xu *et al.* [115] designed a silver ion-mediated chiral plasma assembly for DNA recognition (Fig. 11C). The assembly consisted of two different sizes of DNA-functionalized Au NPs, and when the two DNA-functionalized Au NPs were mixed in a sample solution containing the target silver ion, the Ag ion-driven recognition process facilitated the assembly of the two types of Au NPs into a heterodimer. This assembly significantly increased the chiral optical activity of the solution, and a significantly enhanced CD signal was detected in the visible wavelength range. The LOD for the detection of $Ag^{+}$ by this method was 2 pmol/L.

Moreover, Abbasi and Khani *et al.* [116] induced side-by-side or end-to-end assembled dimers Au NRs of Au nanoparticles *via* L-Cys (Fig. 11D). Due to the coupling between the surface plasmon resonance of the Au nanoparticles and the chiral signal of L-Cys, the Au NRs have a pronounced PCD response. In the presence of $Cu^{2+}$, $Cu^{2+}$ catalyzed the oxidation of Cys to cystine. With increasing $Cu^{2+}$ concentration, the L-Cys-mediated assembly of Au nanoparticles decreased and the PCD signal decreased. Using this property, $Cu^{2+}$ can be detected in the concentration range of 20 pmol/L-5 nmol/L with LOD for 7 pmol/L.

### 3.1.6. Drug molecules detection

Many drugs are composed of organic molecules, mostly chiral [117]. Clinical studies have shown that the pharmacologic effects of two drug enantiomers are generally different: one enantiomer is practical while the other is less effective or has side effects [118]. Therefore, identification of drug enantiomers for clinical use is necessary. The Enantioselectivity of chiral-based inorganic nanomate-

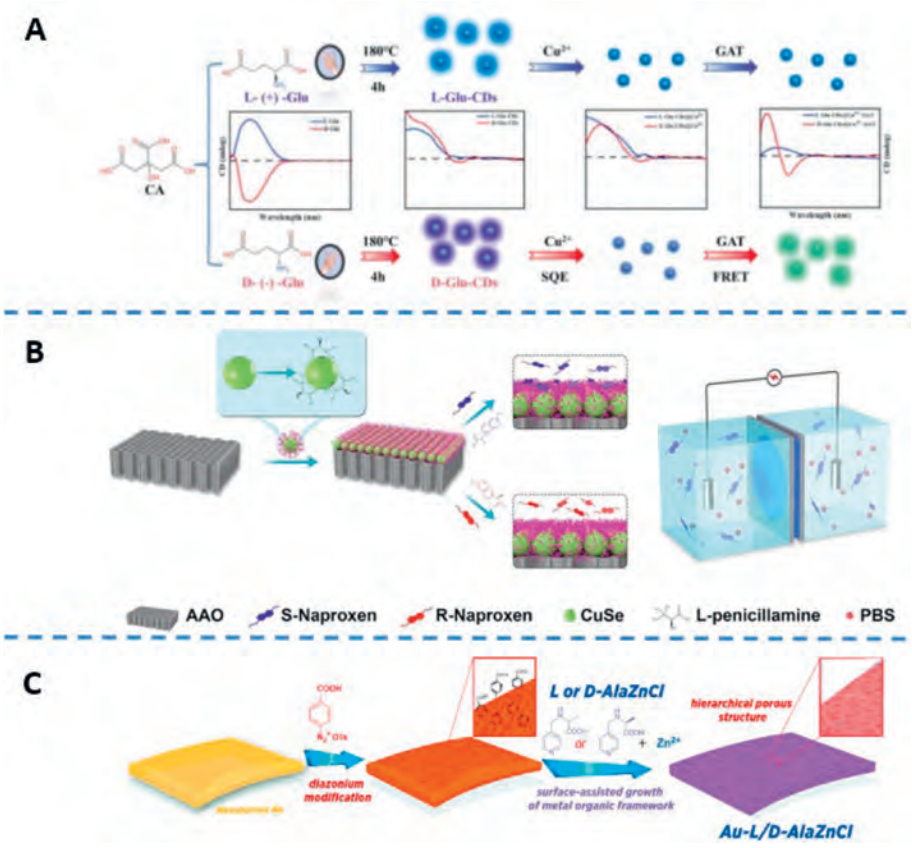



**Fig. 12.** Chiral inorganic nanomaterials for enantioselective detection of drug molecules. (A) Schematic of the synthesis process of L-/D-Glu-CDs and the response of L-/D-Glu-CDs@$Cu^{2+}$ to GAT in fluorescence spectra. Reproduced with permission [119]. Copyright 2022, Elsevier B.V. (B) Fabrication of achiral penicillamine-modified $Cu_{2-x}Se$/AAO heterostructure membrane nanochannel for enantioselective detection of naproxen based on the electrochemical system. Reproduced with permission [120]. Copyright 2021, Wiley-VCH GmbH. (C) Schematic diagram showing the preparation of hierarchical porous AlaZnCl-Au films. Reproduced with permission [121]. Copyright 2021, Elsevier B.V.

rials enables the chiral differentiation of drugs, which is detected by fluorescence, current, and SERS signals. For example, Anli *et al.* [119] utilized a novel chiral rate fluorescent probe constructed from D-Glu-CDs with $Cu^{2+}$ for Förster resonance energy transfer-based Gatifloxacin (GAT) detection (Fig. 12A). The linear range of GAT was 0.01877–105.1 μg/mL under the optimized parameters, and the detection limit was 0.04995 μg/mL. The method has the advantages of good selectivity, wide linear range, convenience, and rapidity, and it has been successfully applied to the determination of GAT in serum. The method was successfully applied to the detection of GAT in serum.

Additionally, Meng *et al.* [120] constructed a multilayer chiral membrane consisting of chiral penicillamine molecules embedded in copper selenide nanoparticles ($Cu_{2-x}Se$ NPs) for the enantioselective recognition of chiral naproxen (S/R-Npx) (Fig. 12B). The chiral nanomembrane has a good rectification effect in PBS solution, and its rectification ratio reaches 114. The addition of S-Npx attenuates the rectification effect of the channel membrane, while R-Npx has no effect. The linear range and detection limit were 0–106 nmol/L and 0.027 nmol/L, respectively.

Furthermore, Guselnikova *et al.* [121] prepared multilayered and porous hybridized thin films (Au-L/D-AlaZnCl) by combining mesoporous plasmonic Au films with microporous homochiral metal-organic skeletons (Fig. 12C). Ultrasensitive and selective detection of chiral drugs in complex biological samples by SERS signals. The authors tested the interaction of human serum and plasma with Au and Au-L-AlaZnCl to estimate the interference with the analyte signal. Gas chromatography analyzed the prepared samples and compared them with SERS sensor measurements. The excellent agreement between the SERS data and the GC results demonstrated the suitability of graded porous chiral SERS substrates for biosensing. Pseudoephedrine was also detected in undiluted plasma, for example, with a detection value of 10 pmol/L.

In conclusion, chiral inorganic nanomaterials have a distinct function in the detection of a diverse array of biomarkers, including nucleic acids, amino acids, proteins, ROS, metal ions, and drug enantiomers. The detection of biomolecules is facilitated by the stereoselective interactions of chiral biomolecules with either the surface-enhanced Raman scattering-chiral anisotropy of chiral precious metal nanomaterials or the fluorescence anisotropy of chiral semiconductor materials. In optical modes based on chirality, variations in energy or changes in relevant CD values can be utilized to accurately quantify biological components, even at very low concentrations. Furthermore, Table 3 provides a summary of additional instances of chiral inorganic nanomaterials used for biomarker detection [122–131].

### 3.2. Disease therapy

Chiral inorganic nanomaterials have demonstrated many advantages in antimicrobial therapy, antiviral therapy tumor therapy, and neurodegenerative disease therapy due to their chiral optical activity, chiral preference response to organisms, and good biocompatibility [132,133]. Chiral inorganic nanomaterials can utilize their unique optical properties to interact with chiral receptors on bacterial cell walls for selective recognition and binding to bacteria. They can also be used as nanoenzymes to catalyze the generation of ROS from substrates using enzyme-like activity, and these ROS are capable of disrupting the cellular structure and function of bacteria to achieve antibacterial effects [134]. Chiral inorganic

**Table 3**
Chiral inorganic nanomaterials for biomarker detection.

| Biomarkers | Nanomaterials | Detection platform | LOD | Ref. |
|---|---|---|---|---|
| L-Pyr | MIPHs | ECL | 2.4 μmol/L | [122] |
| L/D-Tyr | Cu-TBLeuBpa | ECL | 2–4 nmol/L | [123] |
| Alpha-fetoprotein | L/D-Au NPs dimers | CD | 11 pg/mL | [124] |
| Telomerase | L/D-Au heterodimers | CD | $1.7 \times 10^{-15}$ IU (HeLa cell) | [125] |
| Avian influenza A H4N6 virus | L/D-$MoS_2$ | PL[a] | 7.35 pg/mL | [126] |
| Alkaline phosphatase | L/D-Au NR nanorods | EPR[b] | 28.8 U/L | [127] |
| ATP | Chiral core-shell satellite Au nanostructures | CD | 0.2 mmol/L | [128] |
| Ochratoxin A | DPA/Cys-CdS QDs | CD | 0.037 pg/mL | [129] |
| Glucose | L/D-Cys-$MoO_2$ | CD | 31 μmol/L | [130] |
| $Hg^{2+}$ | L/D-Au NPs | CD | 0.08 nmol/L | [131] |

[a] PL: Photoluminescence;
[b] EPR: Electron paramagnetic resonance.

nanomaterials with chiral preference response in biological systems can improve the specificity of tumor therapy and antiviral therapy. They can also be used for PTT or PDT using chiral optical activity, which kills tumor cells by generating a thermal effect or a photosensitizing response. In addition, chiral inorganic nanomaterials can enhance the body's immune clearance of tumors by stimulating the immune response. Chiral inorganic nanomaterials can depolymerize neurotoxic aggregates, such as amyloid, to reduce neurotoxicity and improve the pathology of neurodegenerative diseases. Similarly, chiral inorganic nanomaterials can also effectively degrade viral nucleic acids and viral core antigens. Moreover, they can be used as neuroprotectants to protect neurons from damage through mechanisms such as anti-oxidative stress and inhibition of neuroinflammation.

### *3.2.1. Antimicrobial therapy*

Chiral inorganic nanomaterials have excellent antimicrobial effects as a new antimicrobial agent [135,136]. Chiral nanomaterials exhibit notable selective antimicrobial characteristics by interacting with the cell wall or membrane of specific microorganisms *via* chiral functional groups on their surfaces. This focused strategy minimizes the dependence on antibiotics, which in turn lowers the risk of resistance development. Inorganic nanomaterials that possess chirality greatly improve the antimicrobial efficacy when compared to their achiral counterparts [43].

For example, Chen *et al*. [37] discussed the antimicrobial properties of chiral Au nanobipyramids and achiral A NPs (L-GBPs, D-GBPs, DL-GBPs, Au NPs) that resemble sea cucumbers (Fig. 13A). The findings indicated that D-GBPs and L-GBPs were effective at eliminating bacteria when exposed to NIR irradiation, achieving *in vitro* mortality rates of 98 % and 70 %, respectively, with D-GBPs demonstrating significantly greater antimicrobial efficacy than L-GBPs. The effects of DL-GBPs and Au-NPs were not as pronounced. Furthermore, *in vivo* studies involving skin infections and sepsis in mice revealed that chiral GBPs could significantly enhance wound healing and reduce the risk of sepsis. Mechanistic investigations revealed that the binding affinity of D-GBPs to *S. aureus* protein A was 12.39 times greater than that of L-GBPs, resulting in increased adsorption of D-GBPs on the *S. aureus* surface. Additionally, the superior photoemission properties of D-/L-GBPs further intensified bacterial death without causing any adverse effects on the skin.

Moreover, Gao *et al*. [135] successfully prepared chiral $TiO_2$ superparticles (L/D-SPs), which exhibited CD absorption at 792 nm, by controlling the solvent polarity to enable the formation of a large number of weak interactions (*e.g.*, hydrogen bonding) between the chiral ligand and $TiO_2$ (Fig. 13C). Under CPL at 808 nm, L/D-SPs induced electron-hole pair separation in $TiO_2$, resulting in the generation of hydroxyl and single-linear oxygen radicals. Antimicrobial tests under NIR CPL showed that the L/D-SPs exhibited excellent antimicrobial properties, with inhibition rates of 99.4 % and 100 % against Gram-positive and Gram-negative bacteria, respectively. The recycling experiments and biocompatibility evaluations of the materials showed that L/D-SPs are stable and safe antimicrobial materials.

On the other hand, Xiang *et al*. [136] investigated the antimicrobial properties of sulfur quantum dots, achiral sulfur nanosheets, and chiral sulfur nanosheets (S, SNSs, L-SNSs, D-SNSs) against both Gram-positive (G+) and Gram-negative (G-) bacteria. The findings indicated that S did not significantly inhibit the growth of either G+ or G- bacteria. In contrast, SNSs were effective in killing methicillin-resistant *Staphylococcus aureus* (G+, MRSA) but did not show a notable inhibitory effect on G- bacteria. The D-His-S-NSs demonstrated a significantly greater inhibitory effect on MRSA compared to S-NSs or L-NSs. Additionally, D-S-NSs were found to be more effective against G+ bacteria than S-NSs or L-NSs. The NSs generated a substantial amount of reactive oxygen species and hydrogen sulfide when incubated with bacteria, leading to damage to the bacterial membrane, disruption of the respiratory chain, and inhibition of ATP production. When applied to MRSA-infected wounds, they significantly enhanced skin healing within just 8 days, indicating promising therapeutic effects on MRSA-infected wounds (Fig. 13B).

Additionally, Wang *et al*. [50] created chiral hexagonal star-shaped cobalt superstructures as well as achiral cobalt superstructures (L-Co SS, D-Co SS, D/L-Co SS). It was discovered that L/D-Co SS exhibits chiral activity across a broad wavelength range from 300 nm to 1300 nm, with g coefficients reaching up to 0.033 and demonstrating superparamagnetism. In an electromagnetic field, L/D-Co SS displayed effective antibacterial properties against *Staphylococcus aureus*, with D-Co SS showing a more pronounced antibacterial effect compared to L-Co SS. Further mechanistic investigations revealed that the amount of reactive oxygen species generated by D-Co SS was 1.59 times greater than that produced by L-Co SS (Figs. 13D and E).

In conclusion, chiral inorganic nanomaterials hold great promise in antimicrobial applications because of their distinctive chiral characteristics, nanoscale benefits, and capacity to diminish inflammatory reactions, offering innovative approaches for anti-infective treatment. Furthermore, Table 4 outlines additional examples of chiral inorganic nanomaterials used in antimicrobials [135–140].

### *3.2.2. Antiviral therapy*

Viruses pose a serious threat to human society. Not only do viruses have an impact on human health, they are also potentially destructive to economic and social stability. Therefore, research and development of antiviral drugs are critical in the biomedical field. Chiral inorganic nanomaterials demonstrate enantioselectivity when interacting with biomolecules, which can affect how cells adhere and internalize these materials. Specifically, chiral inorganic

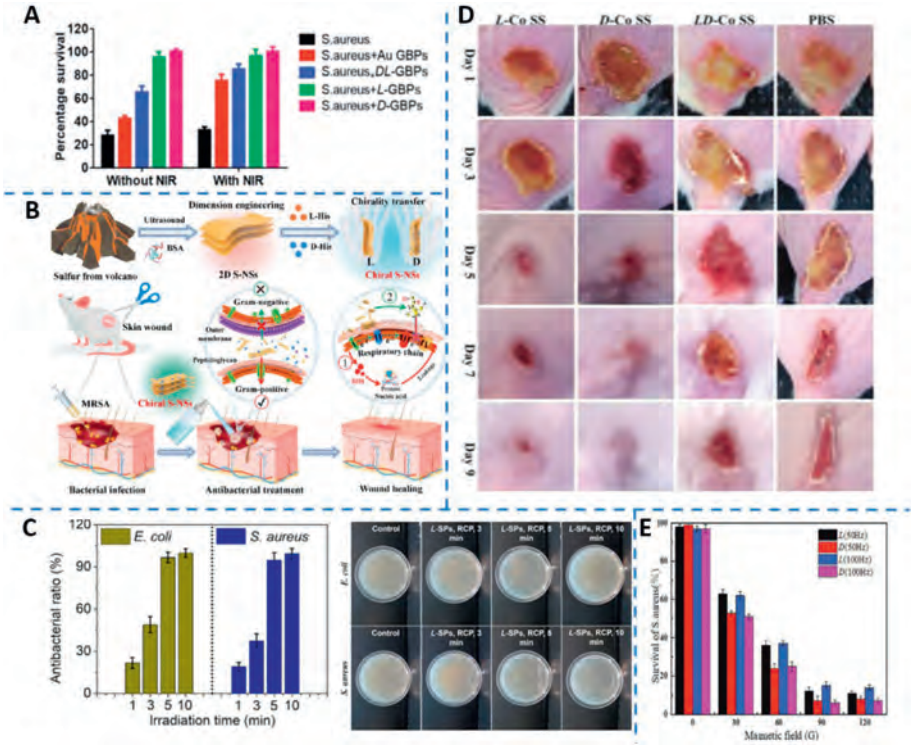



**Fig. 13.** Chiral inorganic nanomaterials for antimicrobial. (A) PBS, DL-GBPs, D-/L-GBPs, and Au NBPs were used to treat the sepsis model. Reproduced with permission [37]. Copyright 2022, Royal Society of Chemistry. (B) Schematic illustration of the preparation process of chiral S-NSs and their dual-selective inhibition of G+ bacteria for accelerating MRSA-infected would healing. Reproduced with permission [135]. Copyright 2024, American Chemical Society. (C) The antibacterial activity of L-SPs under 808 nm RCP for different times and the photos of CFU plating of *E. coli* and *S. aureus* after treatment with L-SPs with the assistance of 808 nm LCP at different times. Reproduced with permission [136]. Copyright 2023, American Chemical Society. (D) Digital photographs of *S. aureus* infection sites on a scarf after treatment with chiral cobalt superstructured nanomaterials. Reproduced with permission [50]. Copyright 2022, Wiley-VCH GmbH. (E) Effect of magnetic field strength (0, 30, 60, 90, and 120 G) and frequency (50 and 100 Hz) of chiral cobalt superstructures on *S. aureus*. Reproduced with permission [50]. Copyright 2022, Wiley-VCH GmbH.

**Table 4**
Chiral inorganic nanomaterials for antimicrobial.

| Materials | Size | Chirality | Strains | Specificities | Ref. |
|---|---|---|---|---|---|
| L/D-$TiO_2$ SPs | 2.5 ± 1.5 μm | $g_{abs}$ = 7.5 × $10^{-2}$ (990 nm) | *E. coli*/*S. aureus* | 808 nm RCP/LCP | [135] |
| L/D-SNSs | 100–300 nm, 5–6 nm | CD = 15 mdeg (212 nm) | MRSA | - | [136] |
| L/D-CuS | 20 nm | CD = 4 mdeg (600 nm) | *E. coli* | 808 nm RCP/LCP | [137] |
| L-CdTe NPs | 4.21 ± 0.4 nm | CD = 10 mdeg (471 nm) | *E. coli* | 405 nm RCP (100 mW/$cm^2$, 30 min) | [138] |
| L/D-Au nanostars | ~200 nm | CD = 26 mdeg (633 nm) | *E. coli*/*S. aureus* | 808 nm RCP/LCP | [139] |
| L/D-Ag nanoclusters | 2.4 ± 0.2 nm | CD = 40 mdeg (280 nm) | *P. aeruginosa* | - | [140] |

nanomaterials enhance cell adhesion and internalization for specific cells more effectively than their achiral counterparts. Consequently, they enable more accurate targeting of cells in antiviral treatments, improving the effectiveness of therapies while minimizing side effects.

For example, Gao *et al.* [141] reported the synthesis of approximately 3 nm chiral copper sulfide nanoparticles and achiral copper sulfide nanoparticles (L-$Cu_{1.96}S$, D-$Cu_{1.96}S$, rac-$Cu_{1.96}S$ NPs) using penicillamine as a ligand, which matched the size and shape of the inner pore of the TMV virus helix. It was discovered that D-$Cu_{1.96}S$ NP had a 20-fold greater affinity for the TMV protein subunit Q99AN^PTTA105 site compared to L-$Cu_{1.96}S$ NP, and over 5000 times greater affinity than the achiral nanoparticles. Utilizing sunlight, the peptide bond between asparagine (Asp, Q) at position 101 and proline (Pro, P) at position 102 of the phage protein is cleaved, resulting in the lysis of the viral phage. This process effectively dismantles the virus's physical barrier, revealing the nucleic acids within the pore, which are subsequently degraded (Fig. 14A). This method of destruction does not target the virus's physiological metabolic pathways, thus preventing viral mutations and eliminating the chance for mutated viruses to evade detection.

Additionally, Guo *et al.* [46] synthesized chiral copper sulfide nanoparticles (L/D-$Cu_2S$ NPs) with a size of 4 ± 0.5 nm, which have a chirality of 46 mdeg at 530 nm, can selectively cleave the core antigen (HBcAg) of hepatitis bvirus (HBV) and can efficiently block the assembly of HBV *in vitro* and *ex vivo* under light irradiation at 808 nm and prevent HBV infection (Fig. 14B). Experimental analysis showed that the L/D-$Cu_2S$ NPs were able to specifically bind the functional domain between phenylalanine 23 (F23) to leucine 30 (L30) in the primary sequence of HBcAg, and their cleavage site was located between amino acid residues F24 and proline 25 (P25). Under 808 nm excitation, (L/D-$Cu_2S$ resulted in a 95% reduction in intracellular HBcAg concentration. In the HBV transgenic mouse model, HBsAg and HBV DNA levels were reduced by 93% and 86% after treatment, respectively.

Moreover, Fan *et al.* [142] prepared three different types of chiral and achiral zincoxide NPs (L-ZnO, D-ZnO, and DL-ZnO) as enantioselective antiviral drugs (Fig. 14C). The results of biocompatibility tests showed significant differences in the cytotoxicity of the three ZnO NPs. Evaluation of porcine reproductive and respiratory syndrome virus (PRRSV) action showed that L-ZnO NPs exhibited

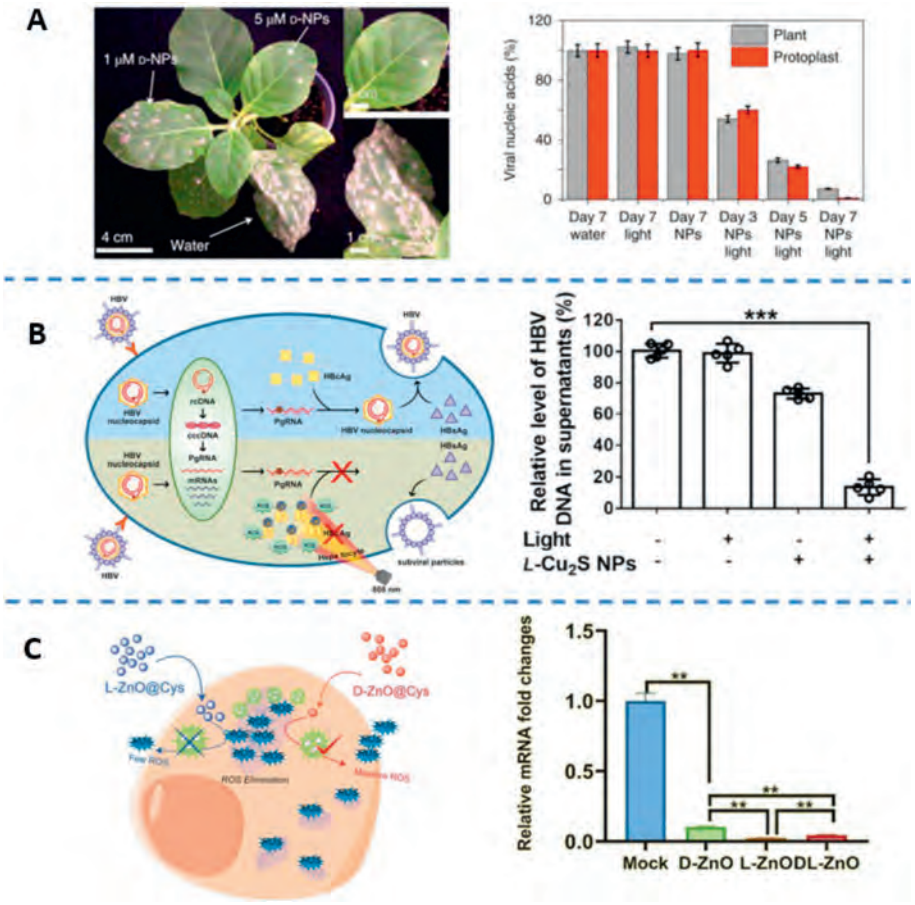



**Fig. 14.** Chiral inorganic nanomaterials for antiviral therapy. (A) Photographs of infected N. tabacum cv. Samsun$^{NN}$ was treated with different concentrations of chiral NP dispersions after three days of spraying under simulated sunlight, and the content of viral nucleic acids was extracted from protoplasts and plants. Reproduced with permission [141]. Copyright 2022, The Author(s), under exclusive licence to Springer Nature Limited. (B) HBcAg cleavage and inhibition of HBV assembly under 808 nm light irradiation and HBV DNA levels in Hep/G2.2.15 cell culture supernatants were measured by real time-polymerase chain reaction (RT-qPCR). Reproduced with permission [46]. Copyright 2021, Wiley-VCH GmbH. (C) Schematic representation of the enantioselective antiviral activity of chiral zinc oxide nanoparticles and RT-qPCR analysis of the ORF7 gene content in PRRSV genomes treated with different chiral ZnO NPs at 15 μg/mL. Reproduced with permission [142]. Copyright 2023, American Chemical Society.

**Table 5**
Chiral inorganic nanomaterials for antiviral therapy.

| Materials | Size | Chirality | Virus/action site | Specificities | Ref. |
|---|---|---|---|---|---|
| L/D-$Cu_2S$ NPs | 4 nm | CD = 46 mdeg (530 nm) | HBV (HBcAg) | 808 nm (200 mW/cm$^2$, 90 min) | [46] |
| L/D-$Cu_{1.96}S$ NP | 3 nm | $g_{abs}$ = 0.25 ± 0.01 (918 nm) | TMV (TMV protein subunits) | 594 nm RCP/LCP (200 mW/cm$^2$, 6 h) | [141] |
| L/D-ZnO NPs | 2.8 ± 0.1 nm | CD (358 nm) | PRRSV (ROS reduction) | - | [142] |
| L/D-CuS NPs | 30 ± 3 nm, 10 ± 1 nm | CD = 118 ± 4 mdeg (630 nm) | SARS-CoV-2 (S protein, subunit S1) | - | [143] |

stronger anti-PRRSV activity due to their higher homologous cell adhesion and uptake than D-ZnO and DL-ZnO NPs. In addition, high concentrations of L-ZnO NPs significantly reduced ROS in MARC-145 cells, thereby effectively preventing PRRSV-induced oxidative damage.

In summary, chiral inorganic nanomaterials have proven to be effective in treating viruses such as TMV, HBV, and PRRSV, indicating their potential for use in antiviral therapies. Furthermore, additional examples of antiviral applications involving chiral inorganic nanomaterials are compiled in Table 5 for further reference [46,141–143].

### 3.2.3. Tumortherapy

Tumor therapy has always occupied a vital research position in biomedicine. Chiral inorganic nanomaterials play an important role in tumor therapy due to their unique effects on biological systems. Chiral inorganic nanomaterials offer two key benefits in cancer treatment [144]. First, they can specifically target chiral molecules, such as amino acids and sugars, within the body. Second, chiral inorganic nanomaterials are much more effective than achiral ones at stimulating the immune system and enhancing immune cell activity [145]. For instance, Li *et al.* [146] successfully synthesized chiral molybdenum oxide nanoparticles (L/D-$MoO_{2.8}$ NPs) used as PTT agent for tumor (Fig. 15A). Under LCP light, the L-$MoO_{2.8}$ NPs exhibited a strong photothermal-induced temperature increase above 28 °C, with a photothermal conversion efficiency of 41.24 %, higher than 25.5 % reported by Fang *et al.* [147] and 40.01 % reported by Hu *et al.* [148]. In contrast, the opposite measurements for L-$MoO_{2.8}$ NPs under RCP and D-$MoO_{2.8}$ NPs under LCP showed relatively lower efficiency. The material photothermally induced apoptosis in tumor cells and significantly reduced cell damage. It was demonstrated to completely dissolve tumors and excrete them *in vivo* within about 10 days, thus eliminating the possibility of long-term toxicity.

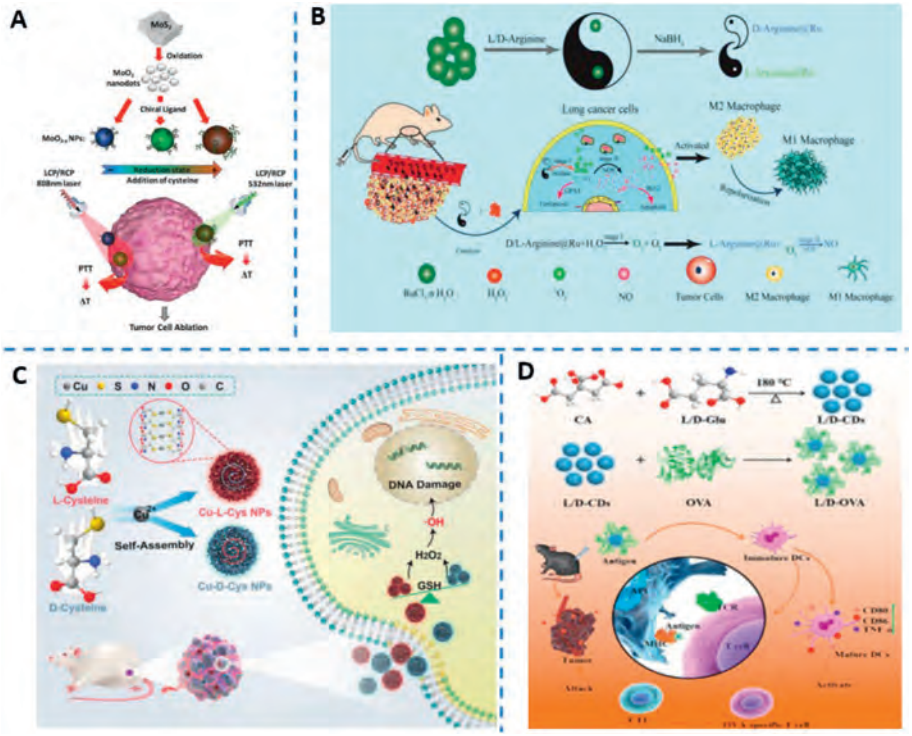



**Fig. 15.** Chiral inorganic nanomaterials for tumor therapy. (A) Synthesis scheme of Cys-$MoO_{3-x}$ NPs and their application in CPL radiation tumor cell ablation. Reproduced with permission [146]. Copyright 2019, Wiley-VCH Verlag GmbH & Co. KGaA, Weinheim. (B) Schematic illustration of the synthesis process of L/D-Arginine@Ru nanoenzymes and the tumor cell inhibitory activity of L/D-Arginine@Ru. Reproduced with permission [149]. Copyright 2023, Wiley-VCH GmbH. (C) Schematic illustration of chiral Cu-L/D-Cys nanoparticles for chiral enhancement of cancer therapeutics. Reproduced with permission [150]. Copyright 2024, Wiley-VCH GmbH. (D) Schematic illustration of L/D-CD and L/D-OVA nanovaccine preparation. Reproduced with permission [152]. Copyright 2023, Wiley-VCH GmbH.

Additionally, Chen *et al.* [149] induced the synthesis of two chiral ruthenium nanoenzymes (L/D-arginine@Ru) with the nitric oxide (NO) precursor arginine (Fig. 15B). The Ru nano enzymes could mimic the activities of oxidase and nitric oxide synthaseby catalyzing the rapid generation of $_1O^2$ from hydrogen peroxide and then catalyzing the production of sufficient NO from arginine, thus enhancing the macrophage M1 polarization and reversing the tumor immunosuppression. Under chiral interaction, L-arginine@Ru has higher natural homology and therefore higher catalytic activity, and also showed better lung cancer therapeutic effects. In tumor tissues, co-stimulation of reactive oxygen species and NO significantly increased the polarization efficiency of macrophage M1. In the study of anti-tumor mechanism, the authors found that L/D-arginine@Ru could induce both apoptosis and iron death and effectively inhibit lung cancer.

Besides, chiral nanomaterials use their own chemical properties for tumor treatment purposes. Wang *et al.* [150] found that Cu-L-Cys chiral NPs have a higher affinity for excess L-GSH produced in cancer cells, which can further improve the efficiency of the Fenton-like reaction, induce cancer cell death, and effectively inhibit tumor growth (Fig. 15C). Both experimental characterization and molecular dynamics simulations verified a stronger interaction between Cu-L-Cys NPs and L-GSH. The strength of this interaction is a crucial factor affecting the rate of the Fenton-like reaction. This study achieves the modulation of catalytic activity and improves therapeutic efficacy by chirality modulating the affinity of nanoparticles for endogenous L-GSH.

Moreover, researchers have also used chiral nanomaterials combined with PDT and CDT to treat tumors. For example, Liu *et al.* [151] researchers synthesized D-/L-Pen modified $Cu_{2-x}Se$ nanoparticles (L/D-NPs) for synergistic enhancement of cancer CDT and PDT under a second NIR light irradiation. Impact studies on the chiral effects on cancer cells showed that D-NPs possessed a stronger capacity for cellular internalisation compared to L-NPs, thus enhancing CDT-induced cytotoxicity. In addition, NIR light irradiation could further ameliorate the hydroxyl radicals produced in D-NPs-treated cancer cells through the PDT effect, thereby increasing apoptosis. *In vivo* experiments have shown that the PDT effect of D-NPs on tumor sites is more significant under NIR conditions.

Chiral inorganic nanomaterials also play an excellent role in inducing immune responses *in vivo*. In this regard, Liu *et al.* [152] researchers successfully prepared a chiral nano vaccine (L/D-OVA) using chiral C dots as carriers and immune adjuvants and ovalbumin (OVA) as an antigenic model (Fig. 15D). This L/D-OVA nano vaccine was efficiently internalized by mouse bone marrow-derived dendritic cells (BMDCs), induced the maturation of BMDCs, and efficiently presented antigens to T cells, thereby inhibiting the growth of B16-OVA melanoma. Notably, Stronger interaction between L-OVA and dendritic cells compared to D-OVA contributes to more effective activation of dendritic cells, leading to infiltration of the tumor site by CD8+ T cells and enhancement of their activity, resulting in better specific tumor cell killing. At the same time, this vaccine can also activate natural killer cells, resulting in their high expression of NKG2D and secretion of large amounts of granzyme B and perforin, which enhances their killing activity without triggering toxicity in the body.

Furthermore, Xu and colleagues [153] successfully prepared chiral Au NPs (L/D-$P^+$NPs) in the presence of L/D-Cys-Phe under CPL illumination. Experiments with mouse bone marrow-derived macrophages and mouse bone BMDCs showed that chiral Au NPs bound to cluster of differentiation 97 (CD97) and epidermal growth factor-like module receptor 1 (EMR1) opened potassium channels, which resulted in the production of immune signaling complex inflammatory vesicles and promoted the maturation of mouse bone marrow-derived dendritic cells. Moreover, *in vivo* and *in vitro* immune responses depended on nanoparticle chirality, suggesting

**Table 6**
Chiral inorganic nanomaterials for tumor therapy.

| Materials | Size | Chirality | Specificities | Animal/cell models | Ref. |
|---|---|---|---|---|---|
| L/D-Arginine@Ru | 150 nm, 100 nm | CD = 150 mdeg (225 nm) | CDT | LLC cells | [149] |
| Cu-L/D-Cys NPs | 80 nm | CD = 10 mdeg (225 nm) | CDT | BALB/c mice (4T1 cells) | [150] |
| L/D-$Cu_{2-x}Se$ NPs | 50 nm | $g_{abs} = 3.5 \times 10^{-3}$ (1080 nm) | PDT+CDT | BALB/c mice (4T1 cells) | [151] |
| L/D-OVA | 2.11 ± 0.41 nm, 2.18 ± 0.48 nm | CD = 4 mdeg (313 nm) | Immunotherapy | C57BL/6 mice (B16-OVA cells) | [152] |
| L/D-Au NPs | 120 nm | $g_{abs} = 0.44$ (727 nm) | Immunotherapy | Mouse BMDCs | [153] |
| L/D-Au NPs | 100 nm | $g_{abs} = 0.44$ (600 nm) | Immunotherapy | C57BL/6 mice (EG7.OVA cells) | [154] |
| L/D-$Cu_xOS$@Fe-MIL-88B-$NH_2$ | 164 nm | CD = 35 mdeg (488 nm) | Cuproptosis and ferroptosis synergistic therapy | C57BL/6 mice (4T1 cells) | [155] |
| L/D-$MoS_2/CoS_2$ | 155.6 nm | CD = 15 mdeg (550 nm) | Generation of ROS regulates tumor-suppressing tumor-associated macrophage polarisation | 4T1 tumor-bearing mice | [156] |
| L/D-CdSe/CdS | 15.5 ± 2.7 nm, 18.9 ± 3.2 nm | $g_{abs} = 0.36 \times 10^{-4}$ (495 nm) | CDT+PDT | BALB/c mice (U251 cells) | [157] |

that nanoscale chirality can regulate immune cell maturation. Finally, L-$P^+$NPs were also 1258-fold more efficient than D-$P^+$NPs as adjuvants for the H9N2 influenza virus vaccine.

In summary, the results presented suggest that chiral inorganic nanomaterials possess chiral and physicochemical characteristics that could be beneficial for targeted therapy and immune stimulation in cancer treatment, offering new possibilities for combating tumors. Furthermore, Table 6 outlines additional uses of chiral inorganic nanomaterials in tumor therapy [149–157].

*3.2.4. Neurodegenerative diseases therapy*

Neurodegenerative diseases are a group of disorders characterized by degenerative damage to nerve cells leading to progressive loss of nerve function, such as Alzheimer's disease (AD) and Parkinson's disease (PD) [158]. Characterized by the accumulation of protein clumps in the brain, these protein aggregates kill brain cells, thus impairing the normal functioning of the nervous system [159]. The current study finds that chiral inorganic nanomaterials can reduce protein aggregation and promote neuronal cell differentiation, significantly enhancing therapeutic efficacy in neurodegenerative diseases [160].

For example, Qu *et al.* [161] have successfully synthesized DNA-bridging chiral gold nanoparticles ($C_{30(d)}S_5$-$C_{20(l)}$ and $C_{30(d)}$-$C_{20(l)}S_5$) with intense optical activity (Fig. 16A). Under the irradiation of circularly polarized light, these nanoparticles can promote the differentiation of neural stem cells to functional neurons. Moreover, under the irradiation of circularly polarized light, by *in situ* injection of the strongly chiral nanoparticles into the brains of mice, the levels of A and P-tau proteins in AD mice were also significantly reduced, and the pathological behaviors of AD mice were restored at the same time.

Besides, Guo *et al.* [162] synthesized gold nanoparticles containing L-, D-, and achiral Au nanoparticles (L-Au NP, D-Au NP, and t-Au NP) and fed the Au nanoparticles to 10-month-old APP/PS1 CE mice at 10 mg $kg^{-1}$ $day^{-1}$ (Fig. 16B). After 90 days, the mice showed significantly improved performance on the Morris water maze cognitive test, with a dramatic reduction in the time required to find the hidden platform, and the mice in the L-Au NP group showed a reduction of more than 70% in the A$\beta$ and P-tau in the cerebrospinal fluid, with the average level dropping to a level similar to that of wild-type mice levels. The team analyzed the gut microbes of the mice and found that the AD mice on L-Au NP had an increase in beneficial bacteria in their intestines, which became close to that of wild-type mice. Further analyzing fecal metabolites in the AD mice, the researchers found that indole-3-acetic acid (IAA) levels increased in the AD mice after oral administration of L-Au NP, and previous studies have shown that IAA can reduce neuroinflammation. Therefore, the study focuses on remodeling gut microbes through oral administration of chiral Au nanoparticles to increase levels of the metabolite IAA, which reduces neuroinflammation and improves cognition.

On the other hand, Shi [163] and his research team prepared chiral L/D-$Cu_xCo_yS$ superparticles (L/D-SPS) (Fig. 16C). Under the irradiation of 808 nm near-infrared light, L/D-SPS prevented the formation of protofibrils from $\alpha$-Syn monomers and induced the transformation of $\alpha$-Syn protofibrils to monomers. In *in vivo* cell experiments, D-SPS significantly reduced cell damage, neuronal dysfunction, and neuronal loss triggered by $\alpha$-Syn protofibrils within just 10 min after irradiation with near-infrared light, thus effectively preventing the aggregation of $\alpha$-Syn. The *in vivo* results showed that D-SPS had a protective effect against neuronal damage induced by anti-$\alpha$-Syn aggregation, alleviating the PD mouse model symptoms and improving cognitive ability. In addition, the $\alpha$-Syn content in the PD mouse model decreased by more than 67.5% after near-infrared light irradiation. Notably, D-SPS could gradually decompose into small nanoparticles within 60 days, excreted through the blood-brain barrier, further improving its therapeutic safety and efficacy.

Furthermore, Jiang *et al.* [164] designed Ptzyme@L-ZIF and Ptzyme@D-ZIF nanoenzymes by encapsulating platinum nanoenzymes (Ptzymes) in chiral lithoimidazolate framework (L/D-ZIF) shells (Fig. 16D). The nanoenzymes exhibited typical ZIF crystal structures and excellent cascade superoxide dismutase and catalase mimetic activities. Compared with Ptzyme@L-ZIFs, Ptzyme@D-ZIFs were more favorable in crossing the blood-brain barrier *in vitro* through lattice protein-mediated and fovea-mediated endocytosis. Ptzyme@D-ZIFs were more stable in plasma and showed more accumulation in the brain. In addition, mouse model experiments demonstrated that Ptzyme@D-ZIFs significantly rescued motor deficits and memory loss in PD mice. The therapeutic effect of Ptzyme@L-ZIFs was significantly less than that of Ptzyme@D-ZIFs, mainly attributed to the reduced blood clearance and optimized distribution of Ptzyme@D-ZIFs *in vivo*. Pathologic data further demonstrated that Ptzyme@D-ZIFs significantly reduced damage to dopaminergic neurons in the substantia nigra pars compactaand increased neuronal density, which prevented aggregation of pathological proteins and alleviated the symptoms of PD.

Collectively, these research findings indicate that chiral inorganic nanomaterials can engage with misfolded proteins, preventing amyloid formation, reducing aggregation, and improving treatment outcomes for neurodegenerative diseases. Furthermore, chiral inorganic nanomaterials have demonstrated remarkable efficacy in PDT, where light-activated chiral nanomaterials generate reac-

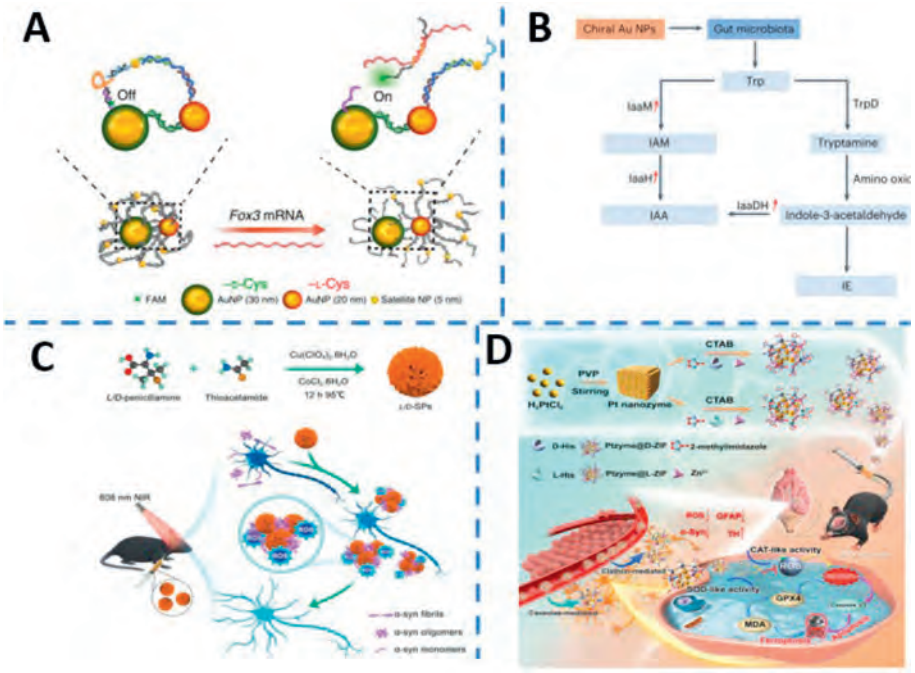



**Fig. 16.** Chiral inorganic nanomaterials for the treatment of neurodegenerative diseases. (A) Schematic representation of the Fox3 mRNA-triggered conformational transition of the $C_{30}$(d)$S_5$-$C_{20}$(l) nanocomponent. Reproduced with permission [161]. Copyright 2020, The Author(s), under exclusive licence to Springer Nature Limited. (B) Mechanism of chiral Au NP-induced IAA, IAM, and IE in Trp metabolism. Reproduced with permission [162]. Copyright 2023, Springer Nature. (C) Illustration of the inhibition and disassembly effects of Chiral $Cu_xCo_yS$ Supraparticles on $\alpha$-Syn aggregation and mitigation of potential neurotoxicity in a PD mice model. Reproduced with permission [163]. Copyright 2022, Chinese Chemical Society. (D) Schematic representation of the therapeutic mechanism of L/D-Ptzymes@ZIFs in Parkinson's disease. Reproduced with permission [164]. Copyright 2023, The Author(s).

**Table 7**
Chiral inorganic nanomaterials for the treatment of neurodegenerative diseases.

| Materials | Size | Chirality | Specificities | Animal/cell models | Ref. |
|---|---|---|---|---|---|
| $C_{30(d)}S_5$-$C_{20(l)}$/$C_{30(d)}$-$C_{20(l)}S_5$ | 30 nm | CD = 37.4 ± 1.4 mdeg (524 nm) | Circularly polarized photons enhance neural stem cells differentiation to neurons | 2xTg-AD mice (neural stem cells) | [161] |
| L/D-Au NPs | 100 nm | CD = 1000 mdeg (590 nm) | modulating gut microbiome and boosting IAA levels | APP/PS1 transgenic AD mice model | [162] |
| L/D-$Cu_xCo_yS$ | 87 ± 6 nm, 89 ± 4.5 nm | CD = ±35 mdeg (830 nm) | Reduce $\alpha$-Syn toxicity and aggregation | PD mice (1-methyl-4-phenyl-1,2,3,6-tetrahydropyridine) | [163] |
| L/D-Ptzymes@ZIFs | 82.24 ± 17.33 nm, 70.37 ± 15.84 nm | $g_{abs}$ = 0.55 (216 nm) | Inhibits neuroinflammation-induced apoptosis and ferroptosis | PD mice (1-methyl-4-phenyl-1,2,3,6-tetrahydropyridine) | [164] |
| UiO-66-NH2@l-$MoS_2$@PA-Ni | 90 nm | CD = 10 mdeg (222 nm) | Enhances neural stem cells differentiation, $H_2$ production, and clears A$\beta$ plaques | Mouse transwell model (Bend.3 cells and PC-12 cells) | [165] |
| L/D-$MoS_2$@cellulose | 20–100 nm | CD = ±25 mdeg (350 nm) | Enhances myelination and stimulates axonal activity | Sprague-Dawley rats | [166] |

tive oxygen species that specifically target and eliminate diseased cells while sparing healthy ones. Additionally, Table 7 provides a summary of various instances where chiral inorganic nanomaterials have been utilized in the treatment of neurodegenerative diseases [161–166].

In conclusion, this chapter highlights the utilization of chiral inorganic nanomaterials for the detection of biomarkers and the treatment of diseases. Regarding biomarker detection, we primarily focus on the identification of various nucleic acids, amino acids, proteins, ROS, metal ions, and drug enantiomers. In the realm of disease treatment, chiral inorganic nanomaterials have been employed in antimicrobial, antiviral, oncological, and neurodegenerative disease therapies. Furthermore, we will explore potential future applications and the technical challenges associated with chiral inorganic nanomaterials in Section IV.

## 4. Conclusions and perspectives

Chiral inorganic nanomaterials, which are nanostructures with unique chiral properties, have attracted the attention of more and more scientists in recent years. Due to their excellent optical properties and good biocompatibility, chiral inorganic nanomaterials have ushered in a wide range of applications in the biomedical field. The chiral nature is widely present in life phenomena, which determines that chiral nanomaterials have a non-negligible role in biological systems. Therefore, developing safe and effective chiral inorganic nanomaterials is significant to the biomedical field. This paper summarizes the chiral synthesis strategies of chiral inorganic nanomaterials and some fundamental research results in marker detection and disease therapy in recent years. It looks forward to their future development prospects.

Although the feasibility and superiority of chiral inorganic nanomaterials in disease diagnosis and treatment have been reported, the relevant research is still in the preliminary stage in the biomedical field. Many problems still need to be solved:

(1) The chiral sizes of different types and sizes of inorganic nanomaterials are not comparable, and it is not clear how chirality affects the changes in the biological environment at different levels when chiral inorganic nanomaterials interact with biological systems, including molecules, cells, tissues, organs, *etc*., which hampers the use of chiral properties for specific clinical applications.
(2) There are fewer studies on detecting chiral inorganic nanomaterials in clinical samples. However, due to the high impurities in clinical specimen samples and the presence of multiple chiral molecules, it is not possible to directly, quantitatively, or qualitatively detect a particular chiral marker in clinical samples, resulting in most of the studies on chiral inorganic nanomaterials remaining in the detection of pure samples with no practical application to clinical samples.
(3) Chiral inorganic nanomaterials' disease treatment mechanism is still unclear. The mechanism of how chiral inorganic nanomaterials regulate immune response and participate in metabolic pathways in organisms has not been well studied.

Despite the above challenges, chiral nanomaterials offer distinct advantages over achiral nanomaterials in numerous areas of biology and medicine. The specific preference and favorable response of biomolecules to chiral materials offer various prospects for their biological applications. The scope of applications in biomedicine can be further broadened by enhancing the study of the properties of chiral nanomaterials and exploring in depth the mechanisms of their interactions with biomolecules or cells.

## Declaration of competing interest

The authors declared that they have no conflicts of interest to this work.

## Acknowledgments

We acknowledge the funding support by the National Science Foundations of China (No. 62471218), the Key Research and Development Project of Jiangsu Province (Nos. BE2022692 and BE2023652), the Nanjing Important Science & Technology Specific Projects (No. 2021-11005), Nanjing International, Hong Kong, Macao and Taiwan Science and Technology Co-operation Program Project (No. 202308001), Nanjing Science and Technology Development Plan Project (No. 202205066).

## References

[1] L. Xiao, T. An, L. Wang, et al., Nano Today 30 (2020) 100824.
[2] V.A. Pavlov, E.I. Klabunovskii, Russian Chem. Rev. 84 (2015) 121–133.
[3] Q. Sallembien, L. Bouteiller, J. Crassous, M. Raynal, Chem. Soc. Rev. 51 (2022) 3436–3476.
[4] Y. Zhou, S. Wu, H. Zhou, et al., Environ. Int. 121 (2018) 523–537.
[5] J. Guo, Y. Duan, Y. Jia, et al., Nat. Commun. 139 (2024) 41467–43700.
[6] J. Guo, S. Kong, Y. Lian, M. Zhao, Chem. Commun. 60 (2023) 918–934.
[7] P. Sutter, L. Khosravi-Khorashad, C.V. Ciobanu, E. Sutter, Mater. Horiz. 10 (2023) 3830-3839.
[8] G. Wang, A. Qu, M. Sun, et al., Acc. Mater. Res. 5 (2024) 1221–1236.
[9] Y. Li, Q. Li, X. Miao, et al., Angew. Chem. Int. Ed. 60 (2020) 6744–6751.
[10] Z. Wang, Q.P. Zhang, F. Guo, et al., Nat. Commun. 670 (2024) 41467–44922.
[11] S. Zhang, Y. Zheng, H. An, et al., Angew. Chem. Int. Ed. 57 (2018) 16754–16759.
[12] X. Gao, X. Yang, J. Lv, et al., J. Am. Chem. Soc. 146 (2024) 14697–14704.
[13] S. Li, X. Xu, L. Xu, et al., Nat. Commun. 15 (2024) 41467–47657.
[14] B. Ma, A. Bianco, Nat. Rev. Mater. 8 (2023) 403–413.
[15] G. Wang, H. Zhang, H. Kuang, et al., Matter 6 (2023) 1752–1781.
[16] C. Hao, C. Xu, H. Kuang, Chem. Commun. 59 (2023) 12959–12971.
[17] Y. He, X. Zhang, F. Meng, et al., Adv. Funct. Mater. 34 (2023) 2313157.
[18] T. Guan, Y. Liu, J. Li, et al., Chem. Eng. J. 474 (2023) 145429.
[19] Y. Zhou, R.L. Marson, G. van Anders, et al., ACS Nano 10 (2016) 3248–3256.
[20] K. Cao, Y. Du, J. Lin, C. Cai, Macromolecules 57 (2024) 6514–6521.
[21] W. Wang, W. Wang, Y. Chen, et al., ACS Nano 18 (2024) 18257–18281.
[22] S. Bera, B. Xue, P. Rehak, et al., ACS Nano 14 (2020) 1694–1706.
[23] W. Ma, L. Xu, A.F. de Moura, et al., Chem. Rev. 117 (2017) 8041–8093.
[24] J. Lin, R. Liu, X. Zhu, et al., Small 18 (2022) 2107570.
[25] Y.H. Kwon, Y.A. Joh, B.M. Leonard, et al., J. Colloid Interf. Sci. 642 (2023) 771–778.
[26] J. Hao, Y. Li, J. Miao, et al., ACS Nano 14 (2020) 10346–10358.
[27] V.A. Kuznetsova, E. Mates-Torres, N. Prochukhan, et al., ACS Nano 13 (2019) 13560–13572.
[28] Y.H. Kim, R. Song, J. Hao, et al., Adv. Funct. Mater. 32 (2022) 2200454.
[29] K.P.P. Praveen, K. Myung-Ki, L. Dong-Kwon, Adv. Opt. Mater. 11 (2023) 2301503.
[30] Z. Cao, J. He, C. Jiao, et al., J. Phys. Chem. Lett. 14 (2023) 2533–2541.
[31] X. Liu, Y. Du, S. Wang, et al., Small 19 (2023) 2205187.
[32] H.E. Lee, H.Y. Ahn, J. Mun, et al., Nature 556 (2018) 360–365.
[33] B.L. Li, J.J. Luo, H.L. Zou, et al., Nat. Commun. 13 (2022) 7289.
[34] M. Xiqi, C. Duo, Z. Zhixiong, et al., Nano Res. 16 (2022) 12066–12075.
[35] S. Hrapovic, C.F. Martinez-Farina, J. Sui, et al., Carbohyd. Polym. 298 (2022) 120108.
[36] Z. Mu, T. Shen, H. Deng, et al., ACS Nano 18 (2024) 5051–5067.
[37] P. Chen, G. Wang, C. Hao, et al., Chem. Sci. 13 (2022) 10281–10290.
[38] Z. Yonglong, W. Qian, S. Yiwen, et al., Adv. Opt. Mater. 11 (2023) 2202858.
[39] S. Mokashi-Punekar, T.R. Walsh, N.L. Rosi, J. Am. Chem. Soc. 141 (2019) 15710–15716.
[40] Y.Y. Xie, X.T. Qin, J. Zhang, et al., J. Colloid Interf. Sci. 622 (2022) 135–146.
[41] M. Sujith, E.K. Vishnu, S. Sappati, et al., J. Am. Chem. Soc. 144 (2022) 5074–5086.
[42] M. Zhang, W. Zhang, X. Fan, et al., Nano Lett. 22 (2022) 7203–7211.
[43] M. Zhang, H. Zhang, J. Feng, et al., Chem. Engin. J. 393 (2020) 124778.
[44] J. Cai, A.A. Liu, X.H. Shi, et al., J. Am. Chem. Soc. 145 (2023) 24375–24385.
[45] Y. Li, J. Cheng, J. Li, et al., Angew. Chem. Int. Ed. 57 (2018) 10236–10240.
[46] X. Guo, M. Sun, R. Gao, et al., Angew. Chem. Int. Ed. 133 (2021) 13183–13190.
[47] F. Zhu, J. Wang, S. Xie, et al., Anal. Chem. 92 (2020) 12040–12048.
[48] C. Wang, G. Yuan, C. Wang, et al., Small Struct. 4 (2023) 2200405.
[49] Y. Gu, Y. Du, W. Wang, et al., Chem. Eng. J. 472 (2023) 144873.
[50] G. Wang, C. Hao, C. Chen, et al., Small 18 (2022) 2204219.
[51] J. Kuno, Y. Imamura, M. Katouda, et al., Angew. Chem. Int. Ed. 57 (2018) 12022–12026.
[52] J.Y. Kim, N.A. Kotov, Science 365 (2019) 1378–1379.
[53] L. Yang, C.S. Kwan, L. Zhang, et al., Adv. Funct. Mater. 29 (2019) 1807307.
[54] P. Kumar, T. Vo, M. Cha, et al., Nature 615 (2023) 418–424.
[55] J. Lv, X. Gao, B. Han, et al., Nat. Rev. Chem. 6 (2022) 125–145.
[56] H. Li, E.J. Cornel, Z. Fan, J. Du, Chem. Sci. 13 (2022) 14179–14190.
[57] J. Yan, W. Feng, J.Y. Kim, et al., Chem. Mater. 32 (2019) 476–488.
[58] J. Del Pino, J.J. Slim, E. Verhagen, Nature 606 (2022) 82–87.
[59] R. Barczyk, L. Kuipers, E. Verhagen, Nat. Photonics 18 (2024) 574–579.
[60] C. Hao, G. Wang, C. Chen, et al., Nano-Micro Lett. 15 (2023) 39.
[61] J. Qin, L. Deng, T. Kang, et al., ACS Nano 14 (2020) 2808–2816.
[62] K.J. Jeong, D.K. Lee, V.T. Tran, et al., ACS Nano 14 (2020) 7152–7160.
[63] C. Wu, Q. Fan, Z. Li, et al., Mater. Horiz. 11 (2023) 680–687.
[64] S. Jiang, N.A. Kotov, Adv. Mater. 35 (2022) 2108431.
[65] Y. Liu, P. Xing, Adv. Mater. 35 (2023) 2300968.
[66] C. Hao, Y. Gao, D. Wu, et al., Adv. Mater. 31 (2019) 1903200.
[67] Z. Yang, Y. Wei, J. Wei, Z. Yang, Nat. Commun. 13 (2022) 5844.
[68] M. Kim, M.J. Han, H. Lee, et al., Angew. Chem. Int. Ed. 62 (2023) e202305646.
[69] X. Zhang, Y. Xu, C. Valenzuela, et al., Light: Sci. Appl. 11 (2022) 223.
[70] S. Tannir, L. Levintov, M.A. Townley, et al., Chem. Mater. 32 (2020) 2272–2281.
[71] D. Vila-Liarte, N.A. Kotov, L.M. Liz-Marzán, Chem. Sci. 13 (2021) 595–610.
[72] R. Wang, G. Zhang, H. Liu, Current Opin. Colloid Interf. Sci. 38 (2018) 329–337.
[73] Z. Chen, C.K.K. Choi, Q. Wang, ACS Appl. Mater. Interfaces 10 (2018) 26835–26840.
[74] X. Lan, T. Liu, Z. Wang, et al., J. Am. Chem. Soc. 140 (2018) 11763–11770.
[75] S.H. Suh, Y. Xing, A. Rottensteiner, et al., Nano Lett. 23 (2023) 4439–4447.
[76] F. Liu, Q. Jiang, Q. Liu, et al., CCS Chem. 3 (2020) 985–993.
[77] T. Zhang, B. Wei, J. Am. Chem. Soc. 143 (2021) 16693–16699.
[78] G. Ghosh, R. Barman, A. Mukherjee, et al., Angew. Chem. Int. Ed. 61 (2021) e202113403.
[79] K. Klinker, O. Schäfer, D. Huesmann, et al., Angew. Chem. Int. Ed. 56 (2017) 9608–9613.
[80] J. Lu, K. Bernardino, N.N. Zhang, et al., Science 371 (2021) 1368–1374.
[81] J. Liu, J. Zhang, L. Zhang, et al., Sci. China Chem. 66 (2022) 228–241.
[82] X. Mao, Z. Wang, D. Zeng, et al., ACS Nano 14 (2019) 1208.
[83] Y. Bi, C. Cheng, Z. Zhang, et al., J. Am. Chem. Soc. 145 (2023) 8529–8539.
[84] J.Y. Kim, J. Yeom, G. Zhao, et al., J. Am. Chem. Soc. 141 (2019) 11739–11744.
[85] K. Saito, T. Tatsuma, Nano Lett. 18 (2018) 3209–3212.
[86] Y. Su, Y. Zhang, Z. Ye, et al., Adv. Funct. Mater. 34 (2024) 2403629.
[87] M. Golla, S.K. Albert, S. Atchimnaidu, et al., Angew. Chem. Int. Ed. 58 (2019) 3865–3869.
[88] J.Y. Zhang, B.B. Yang, Y.D. Yang, et al., Ultrason. Sonochem. 86 (2022) 106007.
[89] Y. Liu, Z. Wu, D.W. Armstrong, et al., Nat. Rev. Chem. 7 (2023) 355–373.
[90] J. Zhou, J. Gu, X. Sun, et al., Adv. Sci. 11 (2024) 2308493.
[91] Z. Huang, X. Huang, Y. Zhang, et al., Chem. Engin. J. 497 (2024) 154618.
[92] I.V. Jani, T.F. Peter, Clin. Infect. Dis. 75 (2022) 723–728.

[93] M. Li, F. Yin, L. Song, et al., Chem. Rev. 121 (2021) 10469–10558.
[94] W. Ma, H. Kuang, L. Xu, et al., Nat. Commun. 4 (2013) 2689.
[95] M. Cui, Q. Zhao, Q. Zhang, et al., Anal. Chim. Acta 1038 (2018) 41–51.
[96] T. Funck, F. Nicoli, A. Kuzyk, T. Liedl, Angew. Chem. Int. Ed. 57 (2018) 13495–13498.
[97] Z. Yu, L. Pan, X. Ma, et al., Biosensor. Bioelectron. 237 (2023) 115526.
[98] Z. Liu, X. Li, H. Masai, et al., Sci. Adv. 7 (2021) eabe4365.
[99] Y. Tang, X. Zhong, S. Yan, et al., Angew. Chem. Int. Ed. 60 (2021) 19648–19652.
[100] Q. Zhao, J. Yang, J. Zhang, et al., Anal. Chem. 91 (2019) 12546–12552.
[101] H. Kong, X. Sun, L. Yang, et al., Anal. Chem. 92 (2020) 14292–14296.
[102] W. Jiang, R. He, H. Lv, et al., ACS Sens. 8 (2023) 4264–4271.
[103] R. Kehm, T. Baldensperger, J. Raupbach, A. Höhn, Redox Biol. 42 (2021) 101901.
[104] Y. Wang, Z. Rao, J. Zhou, et al., Biosensor. Bioelectron. 132 (2019) 84–89.
[105] G. Wang, C. Hao, W. Ma, et al., Adv. Mater. 33 (2021) 2102337.
[106] B. Yang, Y. Chen, J. Shi, Chem. Rev. 119 (2019) 4881–4985.
[107] F. Yan, Y. Zang, J. Sun, et al., Trend. Anal. Chem. 131 (2020) 116009.
[108] D. Kalyane, D. Choudhary, S. Polaka, et al., Progress Mater. Sci. 130 (2022) 100974.
[109] H. Yang, R.M. Villani, H. Wang, et al., J. Experim. Clin. Cancer Res. 37 (2018) 266.
[110] B. Cao, H. Zhang, M. Sun, et al., Adv. Mater. 36 (2022) 2208037.
[111] C. Hao, X. Wu, M. Sun, et al., J. Am. Chem. Soc. 141 (2019) 19373–19378.
[112] A. Qu, Q. Chen, M. Sun, et al., Adv. Mater. 36 (2024) e2308469.
[113] C. Hao, L. Xu, M. Sun, et al., Adv. Funct. Mater. 28 (2018) 1802372.
[114] X. Wang, J. Hao, J. Cheng, et al., Nanoscale 11 (2019) 9327–9334.
[115] Z. Xu, L. Xu, L.M. Liz-Marzán, et al., Adv. Opt. Mater. 1 (2013) 626–630.
[116] S. Abbasi, H. Khani, Spectrochim. Acta Part A: Mol. Biomol. Spectro. 186 (2017) 76–81.
[117] B. Chankvetadze, Trend. Anal. Chem. 143 (2021) 116332.
[118] J.C. Barreiro, M.E. Tiritan, Q.B. Cass, Trend. Anal. Chem. 142 (2021) 116326.
[119] C. Anli, L. Renjie, Z. Yujia, et al., Sensor. Actuator. B: Chem. 359 (2022) 131602.
[120] D. Meng, C. Hao, J. Cai, et al., Angew. Chem. Int. Ed. 60 (2021) 24997–25004.
[121] O. Guselnikova, H. Lim, J. Na, et al., Biosensor. Bioelectron. 180 (2021) 113109.
[122] X. Qiu, Y. Li, Y. hua, et al., Spectrochim. Acta Part A: Mol. Biomol. Spectro. 283 (2022) 121719.
[123] R. An, Q.Y. Hu, L.Y. Song, et al., Inorg. Chem. Front. 11 (2024) 2402–2412.
[124] H. Zhao, S. Bian, Y. Yang, X. Wu, Microchim. Acta 184 (2017) 1855–1862.
[125] M. Sun, L. Xu, P. Fu, et al., Adv. Funct. Mater. 26 (2016) 7352–7358.
[126] S.R. Ahmed, S. Neethirajan, Global Challenges 2 (2018) 1700071.
[127] Y. Chen, S. Xia, J. Duan, et al., ACS Appl. Nano Mater. 7 (2024) 1503–1508.
[128] P. Fu, M. Sun, L. Xu, et al., Nanoscale 8 (2016) 15008–15015.
[129] J. Cai, C. Hao, M. Sun, et al., Small 14 (2018) 1703931.
[130] K. Ngamdee, W. Ngeontae, Sensor. Actuator. B: Chem. 274 (2018) 402–411.
[131] X. Wang, Q. Wang, Y. Chen, et al., Photonics Res. 2 (2021) 213–221.
[132] W. Song, X. Wang, S. Nong, et al., Adv. Funct. Mater. 34 (2024) 2402761.
[133] I.E. Kepiro, I. Marzuoli, K. Hammond, et al., ACS Nano 14 (2019) 1609–1622.
[134] Y. Liu, M. Zheng, Z. Xie, Chem. Engin. J. 486 (2024) 150361.
[135] R. Gao, C. Hao, L. Xu, et al., ACS Nano 18 (2024) 641–651.
[136] H. Xiang, L. Chenxin, Z. Wenjie, et al., ACS Nano 17 (2023) 14893–14903.
[137] Y. Du, Y. Gu, W. Wang, et al., J. Colloid Interf. Sci. 663 (2024) 103–110.
[138] W. Wang, C. Hao, M. Sun, et al., Adv. Funct. Mater. 28 (2018) 1805112.
[139] X. Huang, Q. Chen, Y. Ma, et al., Chem. Engin. J. 479 (2023) 147528.
[140] Z. Wang, Y. Tian, J. Hao, et al., ACS Nano 18 (2024) 7253–7266.
[141] R. Gao, L. Xu, M. Sun, et al., Nat. Catal. 5 (2022) 694–707.
[142] X. Fan, C. Ren, K. Ning, et al., ACS Appl. Mater. Interfaces 15 (2023) 58251–58259.
[143] R. Gao, X. Xu, P. Kumar, et al., Proceed. Nat. Acad. Sci. U. S. A. 121 (2024) e2310469121.
[144] W. Zhou, X. Ma, J. Wang, et al., Smart Medicine 1 (2022) e20220036.
[145] R.A. Mustafa, P. Parkkila, J.M. Rosenholm, et al., Smart Medicine 2 (2023) e20230012.
[146] Y. Li, Z. Miao, Z. Shang, et al., Adv. Funct. Mater. 30 (2019) 1906311.
[147] D.K. Roper, W. Ahn, M. Hoepfner, J. Phys. Chem. C 111 (2007) 3636–3641.
[148] H. Zu, Y. Guo, H. Yang, et al., New J. Chem. 42 (2018) 18533–18540.
[149] X. Chen, Y. Yang, G. Ye, et al., Small 19 (2023) e2207823.
[150] S. Wang, Y. Zhao, S. Yao, et al., Small 20 (2024) 2309328.
[151] Y. Liu, H. Li, S. Li, et al., ACS Appl. Mater. Interfaces 13 (2021) 60933–60944.
[152] A. Qu, M. Sun, L. Xu, et al., Small Methods 8 (2023) e2301332.
[153] L. Xu, X. Wang, W. Wang, et al., Nature 601 (2022) 366–373.
[154] W. Wang, J. Zhao, C. Hao, et al., Adv. Mater. 34 (2022) e2109354.
[155] C. Hao, L. Huang, H. Zhang, et al., Adv. Funct. Mater. 34 (2023) 2312795.
[156] Y. Zhang, T. Cui, J. Yang, et al., Angew. Chem. Int. Ed. 62 (2023) e202307076.
[157] J. Hao, D. Hu, P. Chen, et al., Mater. Design 226 (2023) 111653.
[158] D.M. Wilson, M.R. Cookson, L. Van Den Bosch, et al., Cell 186 (2023) 693–714.
[159] B.C. Creekmore, R. Watanabe, E.B. Lee, Ann. Rev. Pathology: Mechan. Disease 19 (2023) 345–370.
[160] Z. Xu, A. Qu, H. Zhang, et al., Chem. Sci. 13 (2022) 6642–6654.
[161] A. Qu, M. Sun, J.-Y. Kim, et al., Nat. Biomed. Eng. 5 (2020) 103–113.
[162] X. Guo, C. Li, J. Zhang, et al., Nat Aging 3 (2023) 1415–1429.
[163] B. Shi, A. Qu, W. Wang, et al., CCS Chem. 4 (2021) 2440–2451.
[164] W. Jiang, Q. Li, R. Zhang, et al., Nat. Commun. 14 (2023) 8137.
[165] T. Huarong, H. Yuqi, D. Shuqing, et al., Small 19 (2023) 2303530.
[166] M. Li, X. Li, Y. Lv, et al., J. Nanobiotechnol. 22 (2024) 337.